



Research paper

Cobalt ferrite nanoparticles with controlled composition-peroxymonosulfate mediated degradation of 2-phenylbenzimidazole-5-sulfonic acid



Abdulaziz Al-Anazi^a, Wael H. Abdelraheem^{a,b}, Changseok Han^a, Mallikarjuna N. Nadagouda^c, Labrini Sygellou^d, Michalis K. Arfanis^e, Polycarpos Falaras^e, Virender K. Sharma^f, Dionysios D. Dionysiou^{a,*}

^a Environmental Engineering and Science Program, University of Cincinnati, Cincinnati, OH 45221-0012, United States

^b Chemistry Department, Faculty of Science, Sohag University, Sohag 82524, Egypt

^c Department of Mechanical and Materials Engineering, Wright State University, Dayton, Ohio 45324, United States

^d Foundation of Research and Technology Hellas, Institute of Chemical Engineering and High Temperature Chemical Processes (FORTH/ICE-HT), P.O. Box 1414, GR-26504 Patras, Greece

^e Institute of Nanoscience and Nanotechnology, NCSR Demokritos, 15310 Agia Paraskevi Attikis, Athens, Greece

^f Program of the Environment and Sustainability, School of Public Health, Texas A & M University, 1266 TAMU College Station, TX 77843, United States

ARTICLE INFO

Keywords:

Magnetic Co-ferrite nanoparticles
2-Phenylbenzimidazole-5-sulfonic acid (PBSA)
Advanced oxidation process (AOP)
Sulfate radical
Reaction byproducts

ABSTRACT

Magnetic spinel cobalt ferrite nanoparticles with variable composition ($\text{Co}_x\text{Fe}_{3-x}\text{O}_4$; $x = 0.1, 0.5, 0.7$ and 1.0) were synthesized. The nanoparticles were characterized by various surface techniques. Average sizes and surface areas of ferrites were determined in the ranges of 11–34 nm and 18.5–49.1 m^2/g , respectively. Surface analysis of the nanoparticles confirmed the spinel type structures in which Co(II) incorporated into the crystal lattice. The synthesized catalysts were used to dissociate peroxomonosulphate (PMS) into reactive sulfate radicals ($\text{SO}_4^{\cdot-}$) and further into hydroxyl radicals (HO^{\cdot}) to degrade a target pollutant, 2-phenylbenzimidazole-5-sulfonic acid (PBSA) in absence of heat and light. As the molar ratio of cobalt (i.e., x) in the ferrite catalyst increased from 0.1 to 1.0, PBSA degradation enhanced from 24 to 75% in 240 min. The removal of PBSA increased significantly with the increase in PMS concentration up to 0.1 mM, followed by a decrease at PMS levels of > 0.1 mM. Nitrogen content in PBSA was mineralized by the cobalt ferrite-PMS system mostly into NO_3^- and NH_4^+ ions with minor formation of NO_2^- . Only 32% TOC removal was observed over a 240 min reaction time, indicating carbon content in PBSA was not completely mineralized. A chemical probe method, based on free radical scavenging, revealed the contribution of both $\text{SO}_4^{\cdot-}$ and HO^{\cdot} species in PBSA degradation. Fifteen reaction intermediates were identified using LC/Q-TOF-ESI-MS analysis. Hydroxylation, elimination of sulfonate moiety, and ring cleavage processes were involved in the major degradation pathways. Catalyst reuse experiments demonstrated PBSA degradation efficiency either retained or increased with each subsequent reuse. The magnetic spinel Co-ferrite nanoparticles can be applied effectively to activate PMS without energy aiding for degrading harmful emerging organic contaminants in water.

1. Introduction

Homogeneous metal catalysts have been widely used in the treatment of different emerging contaminants in water due to their advantage of solubility in the reaction medium [1,2]. However, the applications of these catalysts in the field of water treatment have drawbacks such as separating the used catalyst from the reaction mixture after use and handling of air-sensitive catalysts in the environment of their applications [3,4]. Among numerous homogeneous materials, first-row transition metals are being investigated for their promising applications, including energy storage,

biomedical applications, and treatment of air and water [5–9]. For example, iron-based spinel metal oxides (or ferrites) have been studied to disinfect and to degrade organics in polluted air and water [10–12]. More recently, interest in cobalt ferrite nanoparticles has been increasing due to their high magnetic anisotropy ($1.8\text{--}3.0 \times 10^5 \text{ J m}^{-3}$ at 300 K), which is important in magnetic recording applications [13]. Cobalt nanoparticles also play an important role in oxygen reduction electrocatalysis and production of highly reactive species to degrade organic contaminants in water [14–16]. The present paper demonstrates the efficient use of cobalt ferrite for the effective degradation of 2-phenylbenzimidazole-5-sulfonic acid (PBSA) in water.

* Corresponding author.

E-mail address: dionysios.d.dionysiou@uc.edu (D.D. Dionysiou).

<http://dx.doi.org/10.1016/j.apcatb.2017.08.054>

Received 20 March 2017; Received in revised form 10 August 2017; Accepted 15 August 2017

Available online 22 August 2017

0926-3373/ © 2017 Elsevier B.V. All rights reserved.

The sunscreen ingredient PBSA is the most frequently used chemical in personal care products (PCPs) due to its ability to absorb ultraviolet (UV) rays [17–19]. It is a water soluble UV absorber and is frequently detected in the environment [19]. Since PBSA and many other organic UV absorbers are endocrine disrupting chemicals in the environment [19], there is a critical need to eliminate such contaminants from water. Degradation of PBSA has been studied using TiO_2 photocatalysis [20] and homogenous photochemical- H_2O_2 [19] processes. In these processes, hydroxyl radical (HO^\bullet) are predominantly generated, causing the degradation of target contaminants. Previous studies demonstrated the essential role of light to irradiate H_2O_2 and activate TiO_2 catalyst systems to decompose PBSA [19–21]. Lately, emphasis on the use of highly reactive sulfate radicals ($\text{SO}_4^{\bullet-}$) to degrade different organic water contaminants was put forth due to its high oxidation potential (i.e., 2.4 V) and attack to certain chemical bonds in organic compounds [16,22–25]. Typically, $\text{SO}_4^{\bullet-}$ can be generated by various techniques such as photolysis, pyrolysis or chemical activation of peroxymonosulfate (PMS) [22,26,27]. Of the various transition metallic ions, a combination of Co^{2+} and PMS has shown superior performance, however, retaining Co^{2+} after use in water is not an easy task. Studies on cobalt-based materials such as magnetic cobalt ferrite nanoparticles are forthcoming [10,28]. Yet, a limited research has been conducted on using these nanoparticles to degrade PBSA in water such as the recent study by Zhang et al. who utilized composite nanomaterial (i.e., nitrogen- and sulfur-co-doped carbon nanotubes-COOH loaded copper ferrite (CuFe_2O_4)) for PBSA degradation [29]. The current study presents, for the first time, the development of simple cobalt ferrite nanomaterial with controlled composition to effectively degrade PBSA in water without additional use of heat or energy. Moreover, the magnetic property of synthesized cobalt ferrite nanoparticles allows the separation of the catalyst using a magnet.

In this study, recyclable magnetic $\text{Co}_x\text{Fe}_{3-x}\text{O}_4$ nanoparticles of variable compositions were synthesized, followed by their detailed characterization using BET surface area analysis and scanning electron microscopy (SEM), selected area electron diffraction (SAED), high resolution transmission electron microscopy (HR-TEM), X-ray diffraction (XRD), X-ray photoelectron spectroscopy (XPS), and Raman spectroscopy techniques. The catalytic activity of synthesized nanoparticles for degrading PBSA was evaluated in the presence of PMS. The study included identification of organic products of PBSA oxidation by liquid chromatography-mass spectrometry (LC-MS) technique in addition to determination of total organic carbon (TOC) and inorganic nitrogen-containing products (NH_4^+ , NO_3^- , and NO_2^-) to learn the mineralization of PBSA by $\text{Co}_x\text{Fe}_{3-x}\text{O}_4$ nanoparticles-PMS system. Finally, proposed reaction pathways, based on identified reaction products and reactivity of involved oxidizing species (HO^\bullet and $\text{SO}_4^{\bullet-}$) are presented.

2. Experimental

2.1. Synthesis of $\text{Co}_x\text{Fe}_{3-x}\text{O}_4$ magnetic nanoparticles

A modified combustion method was used to synthesize cobalt ferrite nanoparticles [30–32]. In this method, a mixture of cobalt(II) acetylacetonate (97%, Sigma Aldrich) and iron(III) chloride (anhydrous, 97%, Fisher Scientific) was initially prepared at a 1:2 molar ratio of cobalt(II) to iron(III). This molar ratio was then varied to produce 4 different stoichiometries where the adequate number of grams of each chemical was determined by multiplying its corresponding ratio by its molecular weight (i.e., $\text{Co}_{0.1}\text{Fe}_{2.9}$, $\text{Co}_{0.5}\text{Fe}_{2.5}\text{O}_4$, $\text{Co}_{0.7}\text{Fe}_{2.3}\text{O}_4$, and $\text{Co}_{1.0}\text{Fe}_{2.0}\text{O}_4$). Polyvinyl alcohol (PVA, 88% hydrolyzed, average molecular weight of 22000) was added to the reaction mixture in a 1:1 ratio by mass. The mixture was grinded and mixed very well with 15 mL Milli-Q water. This mixture was placed in a muffle furnace and then calcined at 500 °C for 30 min causing self-ignition of PVA that ultimately generate magnetic nanoparticles of cobalt ferrite.

To prepare the magnetic cobalt ferrite nanoparticles, a series of different polymers were used. Out of the tested polymers, PVA proved to be the most efficient in synthesizing catalysts with better magnetic properties by hand magnet separation. The alcoholic groups of the PVA

helps to drive the reaction and the gases released stabilize the crystal phase of the cobalt ferrite polymer [33]. Compared to traditional magnetic ferrite synthesis methods, the current procedure is less complicated as it did not require any pretreatment or certain vessels as in hydrothermal methods. The developed method for the nanoparticles synthesis is environmentally friendly due to the use of water and non-toxic, biodegradable polymers. Moreover, no organic solvents or non-biodegradable chemicals (i.e., surfactants) were required for cobalt ferrite preparation which are commonly used in sol-gel techniques [34,35].

2.2. Characterization of $\text{Co}_x\text{Fe}_{3-x}\text{O}_4$ nanoparticles

The resulting $\text{Co}_x\text{Fe}_{3-x}\text{O}_4$ nanoparticles were characterized using several materials characterization methods including SEM, HR-TEM, XRD, XPS and Raman spectroscopy. A JEM-2010F (JEOL) HR-TEM with a field emission gun at 200 kV was used after the samples were prepared in isopropyl alcohol (99.8%, Pharmco), followed by 30 min of ultrasonication (2501R-DH, Branson). Each sample was fixed on a lacey/carbon 300 mesh copper grid (LC325-Cu, EMS). The selected area electron diffraction (SAED) was obtained with low resolution TEM technique and analyzed using the open-source program, Diffraction Ring Profiler. Electron diffraction simulations were performed using the commercial software, Desktop Microscopist, with the input of the well-known space group information.

A Cu-K α wavelength Bruker AXS D8 Discover XRD was used to confirm crystal structure of synthesized samples with a receiving slit of 0.3 and 0.2 scan step size from 10 to 70°. Raman spectroscopy measurements were performed with a Renishaw In-Via Reflex dispersive micro-Raman spectrometer with < 2 cm^{-1} resolution. The laser beam (excitation in the NIR at 785 nm with total laser power below 0.001 $\text{mW}/\mu\text{m}^2$) was focused on a spot of about 6.8 μm in diameter with a x20 magnification lens. Rayleigh scattering was rejected with a 110 cm^{-1} cut-off dielectric edge filter, and analysis of the scattered beam was performed on a 250 mm focal length spectrometer along with suitable diffraction gratings (1200 lines/mm for NIR) and a high-sensitivity charge-coupled device (CCD). All room temperature (RT) Raman spectroscopy measurements were performed in air and at different laser powers to assure that the intensities used did not induce changes in the spectra. The surface analysis studies were performed in a UHV chamber ($P < 10^{-9}$ mbar), equipped with a SPECS LHS-10 hemispherical electron analyzer.

The XPS measurements were carried out at room temperature using unmonochromatized MgK α radiation under conditions optimized for maximum signal (constant ΔE mode with pass energy of 97 eV giving a full width at half maximum (FWHM) of 1.6 eV for the Ag 3d $_{5/2}$ peak of a reference foil). The analyzed area was an ellipsoid with dimensions 2.5 × 4.5 mm^2 . The XPS core level spectra were analyzed using a fitting routine, which allows the division of each spectrum into individual mixed Gaussian-Lorentzian components after a Shirley background subtraction. The samples were pressed in indium foil circular substrate with diameter ~ 1 cm^2 . Wide Scans were recorded for all samples, while the core level peaks that were recorded in detail were: O1s, Fe2p, Co2p and C1s. Errors in our quantitative data are found in the range of ~ 10% (peak areas) while the accuracy for BEs assignments is \pm 0.1 eV.

2.3. Catalytic activity of $\text{Co}_x\text{Fe}_{3-x}\text{O}_4$ nanoparticles

To evaluate the catalytic activity of $\text{Co}_x\text{Fe}_{3-x}\text{O}_4$ ($\text{Co}_{0.1}\text{Fe}_{2.9}\text{O}_4$, $\text{Co}_{0.5}\text{Fe}_{2.5}\text{O}_4$, $\text{Co}_{0.7}\text{Fe}_{2.3}\text{O}_4$ and $\text{Co}_{1.0}\text{Fe}_{2.0}\text{O}_4$), 5.0 mg of catalyst was added to 29 mL Milli-Q water in separate 40 mL glass vials. Sonication for 15 min at 40 kHz (input energy 19 W) was applied to further disperse the catalyst in water. Then, 0.1 mL of 0.2 mM PBSA was added to water containing the catalyst (i.e., final concentration of PBSA = 4.0 μM). To start the reaction, appropriate volumes of a stock solution of PMS (30.0 mM) were added to the solutions based on the final desired concentrations to evaluate the effect

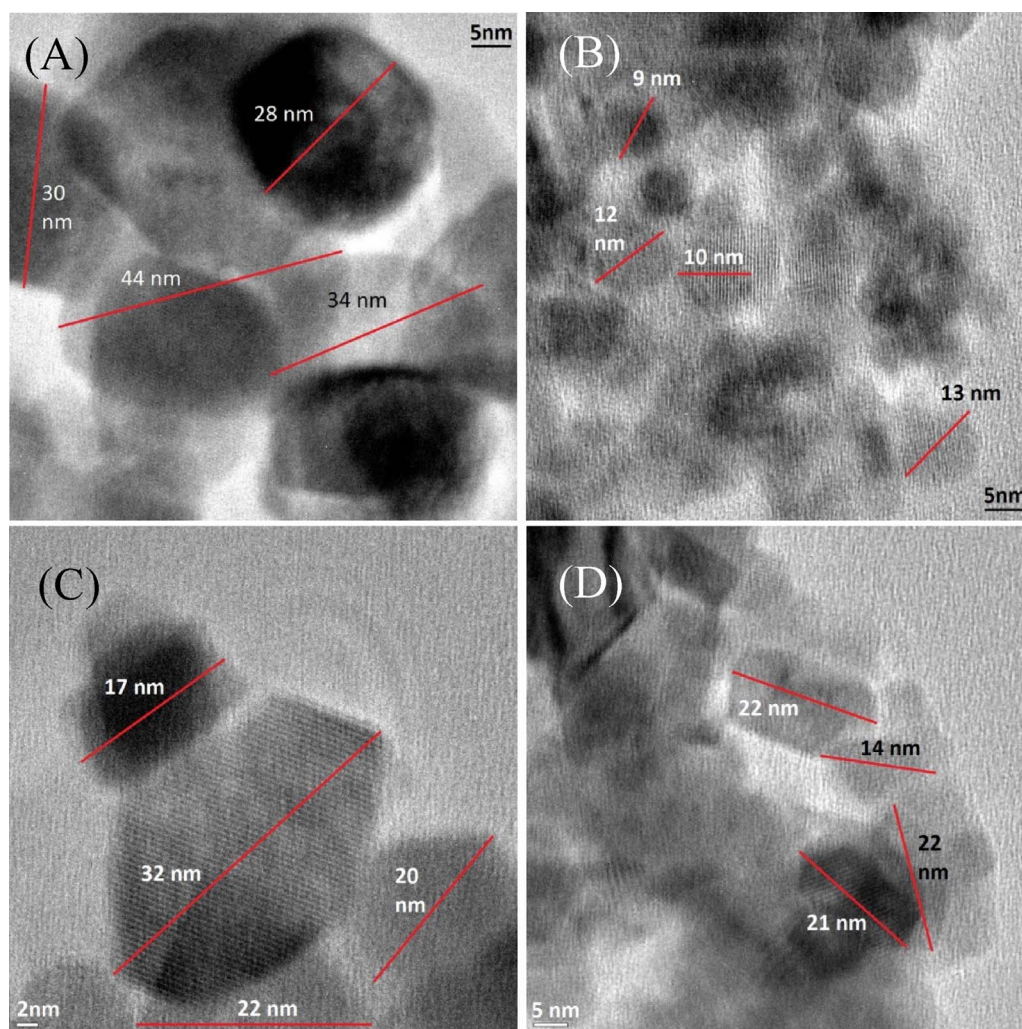


Fig. 1. HR-TEM images of various mixtures of the $\text{Co}_x\text{Fe}_{3-x}\text{O}_4$ samples show crystallized nanoparticles with an average diameter measuring (A) $\text{Co}_{0.1}\text{Fe}_{2.9}\text{O}_4$ (B) $\text{Co}_{0.5}\text{Fe}_{2.5}\text{O}_4$ (C) $\text{Co}_{0.7}\text{Fe}_{2.3}\text{O}_4$ and (D) $\text{Co}_{1.0}\text{Fe}_{2.0}\text{O}_4$.

of PMS concentration for the degradation of PBSA. A final volume of 30 mL was achieved in each vial by addition of appropriate amount of Milli-Q water just before the addition of PMS. The vials were placed in a rotating (50 rpm) vial holder to guarantee complete mixing of the solution during the degradation process. Prior to sampling, the nanoparticles were collected against the wall of vials by using a permanent magnet to minimize the possible loss of catalysts during the consecutive sampling process (Fig. S1). Samples of 500 μL each were drawn at different time intervals (i.e., 0, 15, 30, 60, 120 and 240 min) and were subsequently filtered using a Whatman 0.2 μm syringeless PTFE membrane filter to remove any remaining nanoparticles.

Removal of PBSA by cobalt ferrite-PMS system was performed under dark condition. Vials containing PBSA-ferrite-PMS were wrapped with aluminum foil to block all light to the solution. In order to check the catalyst reusability, nanoparticles collection and regeneration strategies were employed. The suspended nanoparticles were collected at the end of each experiment (Fig. S1) by attaching a magnet to the wall of vials for 1 min. After disposing the solution, the collected nanoparticles were regenerated by washing with Milli-Q water followed by ethanol to remove any leftovers from previous reactions. Finally, the catalyst was dried at 60 $^{\circ}\text{C}$ and then saved in a refrigerator (at $\sim 6^{\circ}\text{C}$) for further reuse.

To investigate the role of HO^{\bullet} and $\text{SO}_4^{\bullet-}$ on the PBSA degradation, a chemical probe method was employed. Experiments at 4 μM PBSA/ 5.0 mg $\text{Co}_{1.0}\text{Fe}_{2.0}\text{O}_4$ /0.1 mM PMS were performed once in the presence of methanol (MeOH) and another time in the presence of *tert*-butanol (*t*-

BuOH) at different concentration levels (i.e., 5, 10, 20 and 100 mM).

Degradation byproducts were identified in experiments conducted at 30 μM PBSA, 0.6 mM PMS and 5.0 mg $\text{Co}_{1.0}\text{Fe}_{2.0}\text{O}_4$ catalyst. Similar experiments were repeated to quantify NO_2^- , NO_3^- , NH_4^+ , and TOC during the degradation experiments.

2.4. Analytical methods

An HPLC (Agilent 1100 Series) with a photodiode array detector (PDA) was used for the quantification of PBSA during the degradation experiments. For separation, a Supelco C_{18} column (150 mm \times 2.1 mm, 5.0 μm) was used with a mobile phase consisted of 0.8% (v/v) acetic acid in water and 100% ethanol at a ratio of 40:60 (v/v), respectively. The flow rate was 0.12 mL min^{-1} , the injection volume of each sample was 10 μL , the column temperature was 25 $^{\circ}\text{C}$, and the detection wavelength for PBSA was set at 286 nm.

Quantification of NO_2^- and NO_3^- released from PBSA during the degradation experiments was performed by using a Dionex Ion Chromatography (model LC20, USA). An IonPac AS18 (2.0 \times 250 mm) column was used to elute the ions. NH_4^+ was measured (as $\text{NH}_3\text{--N}$) using Hach instrument model DR 2800 Spectrophotometer by adjusting the detector to Ammonia Method 8038. A Shimadzu VCSH-ASI TOC Analyzer was used for measurement of the change in total organic carbon (TOC) during the degradation experiments to investigate mineralization of PBSA by the $\text{Co}_x\text{Fe}_{3-x}\text{O}_4$ /PMS system.

An Agilent 1290 infinity HPLC system equipped with a Zorbax

Eclipse XDB-C18 Rapid Resolution column (2.1×50 mm, $3.5 \mu\text{m}$, Agilent Technologies) was used to separate the reaction byproducts from samples taken during PBSA (initial concentration of $30 \mu\text{M}$) degradation experiments. Prior to the analysis, samples were filtrated using Watman Mini-UniPrep PTFE syringeless filters ($0.2 \mu\text{m}$ pore size). The mass analysis of the byproducts was performed by an Agilent 6540 UHD accurate-mass quadrupole time-of-flight tandem mass spectrometer (Q-TOF-MS) which was coupled to the 1290 HPLC with an electrospray ionization source (ESI). Parent compounds and byproduct candidates were identified based on mass to charge ratio (m/z) and isotope distribution. For complete description of the analysis method refer to [21].

3. Results and discussions

3.1. Particle size, crystalline structure, and surface chemistry of $\text{Co}_x\text{Fe}_{3-x}\text{O}_4$

The average particle size of the synthesized $\text{Co}_x\text{Fe}_{3-x}\text{O}_4$ by HR-TEM analysis is shown in Fig. 1. The nanoparticles are of crystalline structures and the average particle size, based on an image processing technique, was found to be 34 nm for $\text{Co}_{0.1}\text{Fe}_{2.9}\text{O}_4$ (Fig. 1A). Fig. 1B shows an average size of 11 nm for $\text{Co}_{0.5}\text{Fe}_{2.5}\text{O}_4$. The average size of $\text{Co}_{0.7}\text{Fe}_{2.3}\text{O}_4$ was 23 nm (Fig. 1C) and of $\text{Co}_{1.0}\text{Fe}_{2.0}\text{O}_4$ was 20 nm (Fig. 1D). The BET surface areas of $\text{Co}_{0.1}\text{Fe}_{2.9}\text{O}_4$, $\text{Co}_{0.5}\text{Fe}_{2.5}\text{O}_4$, $\text{Co}_{0.7}\text{Fe}_{2.3}\text{O}_4$ and $\text{Co}_{1.0}\text{Fe}_{2.0}\text{O}_4$ were determined as 18.5 , 34.1 , 49.2 and $49.1 \text{ m}^2/\text{g}$, respectively.

SEM analysis was also performed on $\text{Co}_{0.1}\text{Fe}_{2.9}\text{O}_4$, $\text{Co}_{0.5}\text{Fe}_{2.5}\text{O}_4$, $\text{Co}_{0.7}\text{Fe}_{2.3}\text{O}_4$ and $\text{Co}_{1.0}\text{Fe}_{2.0}\text{O}_4$ as shown in Fig. S2. There is a very small decrease in particle size with the increase in cobalt concentration in the synthesized nanoparticles. The XRD diffraction data of synthesized cobalt ferrite nanoparticles show peaks at 18° , 30.3° , 35.6° , 37° , 43° , 54° , 57° , and 62.9° which correspond to crystal planes (111), (220), (311), (222), (400), (422), (511) and (440), respectively (Fig. 2). This indicates the cubic spinel type structure for all formulations. The last result compares favorably with the hkl planes of cobalt ferrite that has matching spectra at (111), (220), (311), (222), (400), (422), (511), and (440) (PDF #00-022-1086). The relatively minor peaks of (331), (531), (620), (533), and (622) planes were not observed within the 2θ sweep from 0 to 75° , but all have recorded intensities of less than 10 for pure cobalt ferrite. The percentage of crystal diffraction in proportion to noise floor suggests that the nanoparticles were $\sim 87\%$ crystalline using the Rietveld method [36]. The average size of the crystallites for each of the various formulations was determined at (311) and (222) using the

Scherrer equation (Eq. (1)) [37].

$$\tau = \frac{K\lambda}{\beta \cos \theta} \quad (1)$$

where, $K = 0.9$ (shape factor), λ is the X-ray wavelength 1.5418 \AA , β is the line broadening at FWHM after subtracting instrumental broadening in radians $[\Delta(2\theta)]$, and θ is the Bragg angle of 17.8° . Additionally, peak broadening for the (311) plane was observed when the content of cobalt increased, indicating decrease in crystallite size. Using the dominant (222) peak of $\text{Co}_{0.1}\text{Fe}_{2.9}\text{O}_4$, the Scherrer equation gives an average crystalline size of 35 nm . When cobalt concentration increased in cobalt ferrite like $\text{Co}_{1.0}\text{Fe}_{2.0}\text{O}_4$, the dominant (311) diffraction peak is much broader and an average crystalline size of 9 nm was calculated. Intermediate concentrations of cobalt in $\text{Co}_{0.5}\text{Fe}_{2.5}\text{O}_4$ and $\text{Co}_{0.7}\text{Fe}_{2.3}\text{O}_4$ nanoparticles, obtained crystal sizes are 20 nm and 18 nm , respectively.

Fig. 3(A–D) show SAED patterns of $\text{Co}_x\text{Fe}_{3-x}\text{O}_4$ that have a sequence of diffraction rings; consistent with what is expected for spinel cobalt ferrite as the crystal structure of the nanoparticles [38]. The peaks of $\text{Co}_{0.1}\text{Fe}_{2.9}\text{O}_4$ are (111), (200), (311), (222) and (440) (Fig. 3A), which correspond to cobalt ferrite hkl planes (PDF #00-022-1086). The peaks of $\text{Co}_{0.5}\text{Fe}_{2.5}\text{O}_4$ in Fig. 3B also match with cobalt ferrite with diffraction from planes (111), (220), (311), (400), (511), (440) and (731). $\text{Co}_{0.7}\text{Fe}_{2.3}\text{O}_4$ also resembles cobalt ferrite with diffraction from planes (111), (220), (311), (400), (422), (511) and (440) (Fig. 3C) for. Lastly, $\text{Co}_{1.0}\text{Fe}_{2.0}\text{O}_4$ again agrees very well with cobalt ferrite with diffraction from planes (111), (220), (311), (222), (400), (422), (511), (440), (533) and (731) (Fig. 3D). When measuring the reciprocal space rings in Fig. 3A, the cobalt lattice constants are found to be 0.79 nm for [220], 0.78 nm for [311], 0.78 nm for [400], 0.80 nm for [511] and 0.78 nm for [440]. The average of the lattice constant for $\text{Co}_{0.1}\text{Fe}_{2.9}\text{O}_4$ is evaluated as 0.78 nm . The same analysis is seen for Fig. 3B–D (see Table 1). The lattice constants were calculated using the well-known relationship $d_{hkl} = \frac{a}{\sqrt{h^2 + k^2 + l^2}}$ where d is the interplanar spacing, a represents the lattice constant, and hkl are the Miller indices. It is seen that as the concentration of cobalt increases, the average lattice constant increases from 0.78 nm to 0.84 nm (Table 1).

The results of SAED diffraction rings and XRD lattice plan reflection suggest that the synthesized nanoparticles are cubic crystalline cobalt ferrite in spinel configuration such as AB_2O_4 (see Fig. S3). In this structure, [A] and [B] are occupying the tetrahedral and octahedral sites, respectively [39]. The spinel ferrite unit cell is of cubic structure (space group $\text{Oh}7\text{-F}3\text{dm}$) and forms a cube with eight CoOFe_2O_4

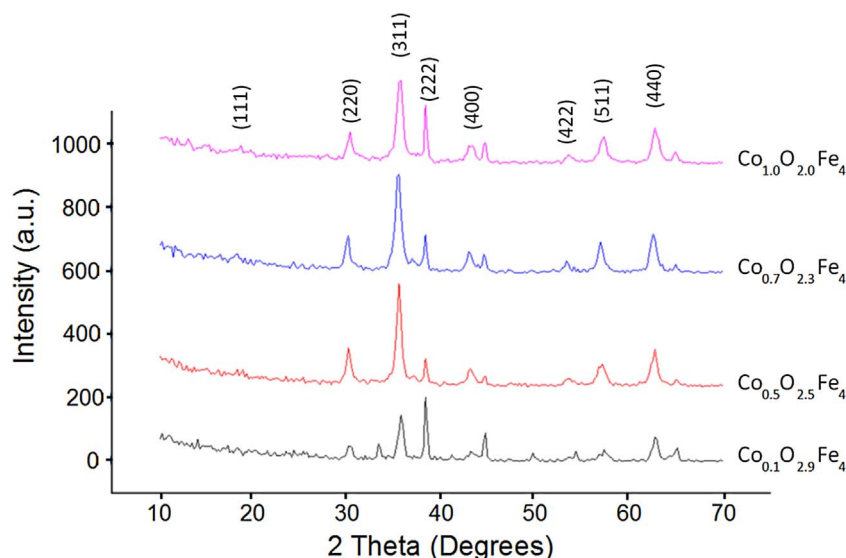


Fig. 2. XRD diffraction patterns of various mixtures of cobalt ferrite spanning from $\text{Co}_{0.1}\text{Fe}_{2.9}\text{O}_4$ to $\text{Co}_{1.0}\text{Fe}_{2.0}\text{O}_4$.

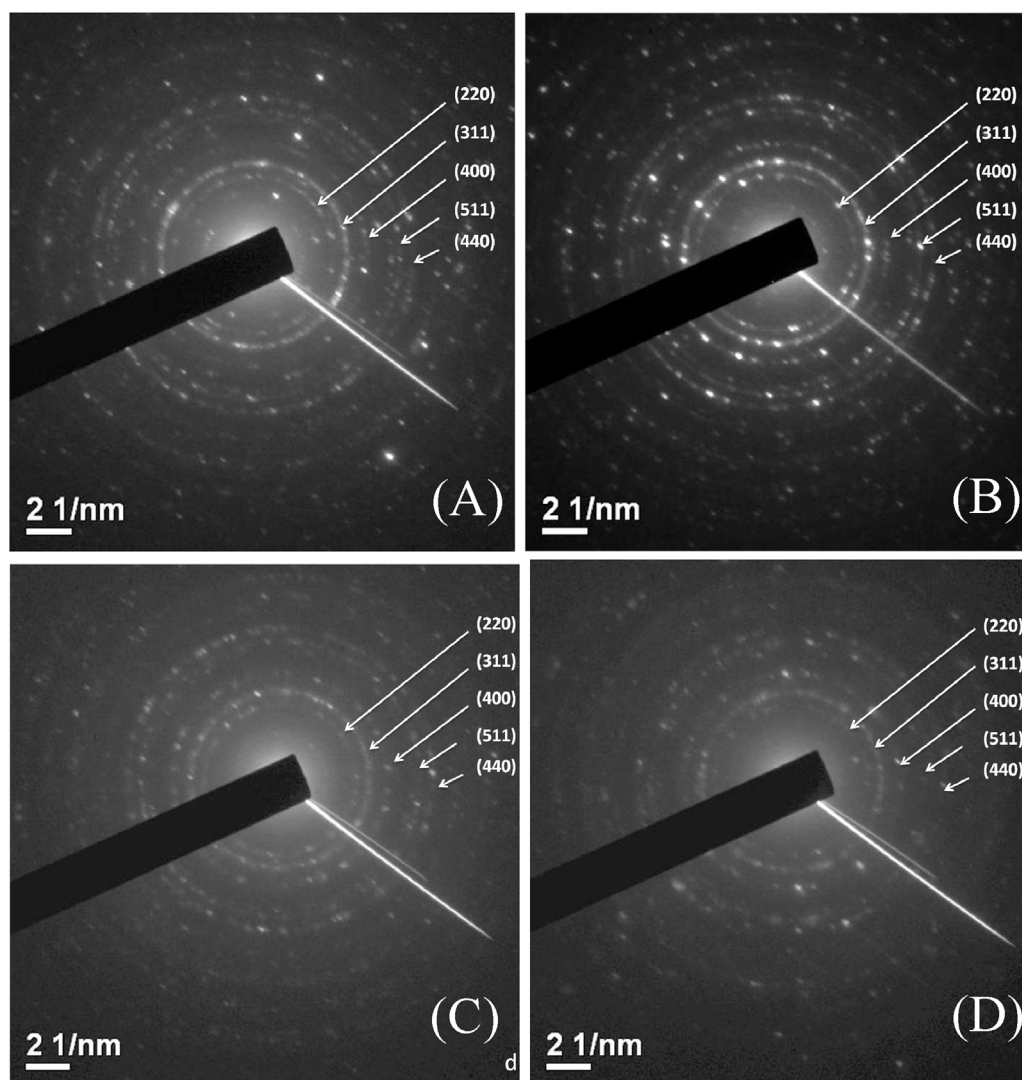


Fig. 3. SAED images of (A) $\text{Co}_{0.1}\text{Fe}_{2.9}\text{O}_4$ (B) $\text{Co}_{0.5}\text{Fe}_{2.5}\text{O}_4$ (C) $\text{Co}_{0.7}\text{Fe}_{2.3}\text{O}_4$ and (D) $\text{Co}_{1.0}\text{Fe}_{2.0}\text{O}_4$.

Table 1

Calculated interplanar lattice spacing and the resulting lattice constant for each of the planes for samples consisting of (A) $\text{Co}_{0.1}\text{Fe}_{2.9}\text{O}_4$ (B) $\text{Co}_{0.5}\text{Fe}_{2.5}\text{O}_4$ (C) $\text{Co}_{0.7}\text{Fe}_{2.3}\text{O}_4$ and (D) $\text{Co}_{1.0}\text{Fe}_{2.0}\text{O}_4$.

Plane	(a) $\text{Co}_{0.1}\text{Fe}_{2.9}\text{O}_4$ (nm)	(b) $\text{Co}_{0.5}\text{Fe}_{2.5}\text{O}_4$ (nm)	(c) $\text{Co}_{0.7}\text{Fe}_{2.3}\text{O}_4$ (nm)	(d) $\text{Co}_{1.0}\text{Fe}_{2.0}\text{O}_4$ (nm)
[220]	0.7919	0.8160	0.7919	0.8249
[311]	0.7803	0.7937	0.8000	0.8291
[400]	0.7770	0.7832	0.8170	0.8057
[511]	0.7950	0.7822	0.8120	0.9447
[440]	0.7764	0.7726	0.7919	0.8040
Mean(nm)	0.7841	0.7895	0.8025	0.8417

molecules consisting of 32 O^{2-} anions. The oxygen anions construct the face-centered cube packing, which consists of 64 tetrahedral (A) and 32 octahedral (B) empty spaces that are partially populated by Fe^{3+} and Co^{2+} cations [40]. In various samples, the cubic spinel ferrites display a high percentage of Fe at the tetrahedral location of 80% [41], 66% [42], and 84% [43]. It appears that the crystal structure alters correspondingly with a shift in percentage of Fe at the tetrahedral site. This accounts the alteration in crystal structure with changing stoichiometry.

The modes in the $\text{Co}_{x-1}\text{Fe}_{3-x}\text{O}_4$ nanoparticles were investigated by Raman spectroscopy, (Fig. 4). The synthesized $\text{Co}_{x-1}\text{Fe}_{3-x}\text{O}_4$ material has four Raman active modes at around 195 (F2 g), 305 (F2 g), 480 (Eg), 620 (F2 g) and 690 cm^{-1} (A1 g) [44]. The position of these vibration modes seems to vary with the synthesis process [44,45] and/or with the incorporation of Co ions in the crystal lattice [46]. In the synthesized cobalt ferrites, the vibrations at the low frequencies (equal or below 490 cm^{-1}) are attributed as vibrations of metal cations and oxygen ions at the octahedral sub-lattice (O-side modes) of $\text{Co}_{x-1}\text{Fe}_{3-x}\text{O}_4$. The vibrations at higher frequencies (620 and 690 cm^{-1}) relates to the vibrations at the tetrahedral sub-lattice (T-side modes) [44–46].

Apart from cobalt ferrites, isolated cobalt and ferrite oxides can also be detected. Significant amount of iron oxide hematite ($\alpha\text{-Fe}_2\text{O}_3$) was present for the lowest content of cobalt ($x = 0.1$), as the vibrational modes at 227, 294, and 414 cm^{-1} are attributed to hematite [47]. By increasing the cobalt content, the samples were well crystallized in the spinel structure with minor traces of impurities. These impurities were randomly formed among the different $\text{Co}_{x-1}\text{Fe}_{3-x}\text{O}_4$ samples, without showing a specific tendency; the broad bands at 520 cm^{-1} (for x equal to 0.7 or 1.0) and 563 cm^{-1} (for x equal to 0.5 or 0.7) are assigned as Co_3O_4 phase [48] and iron oxides [49], respectively.

The elemental compositions of the cobalt ferrites were examined using X-ray photoelectron spectroscopy (XPS). The survey scans of the samples confirmed that Fe, Co, O, and C peaks are present in all cobalt

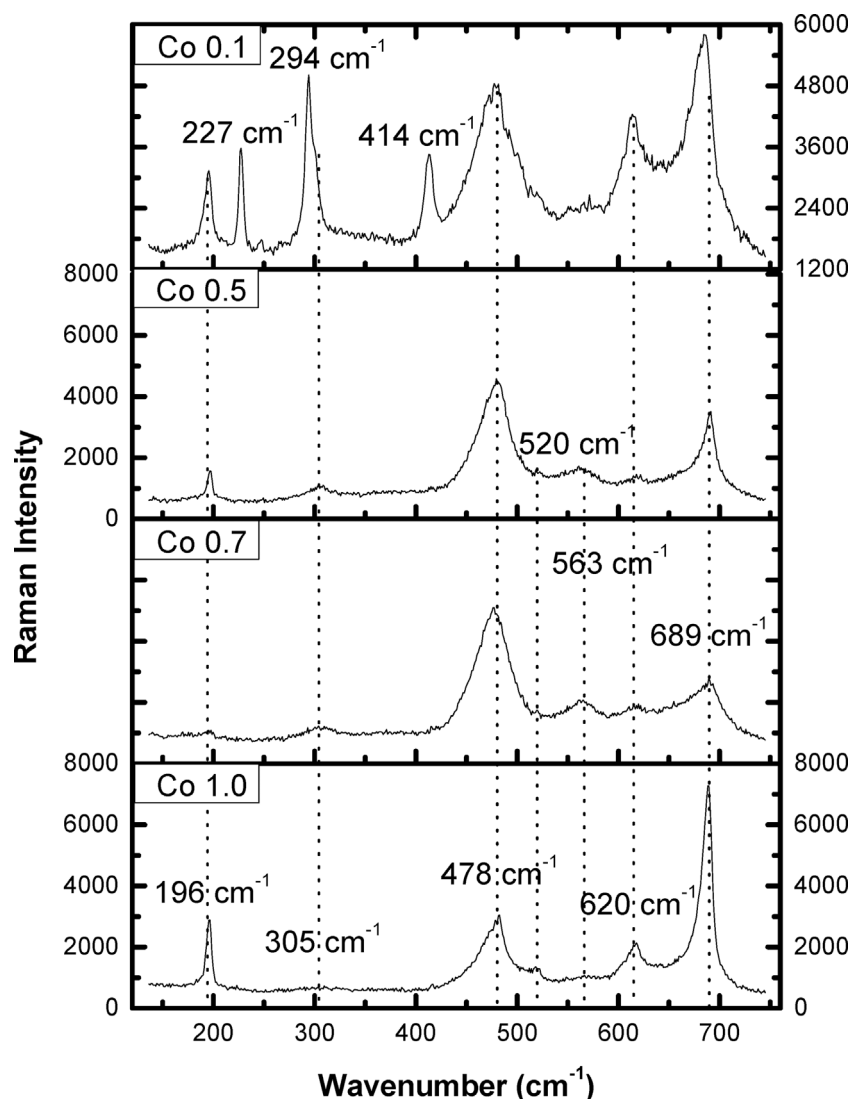


Fig. 4. Raman spectra of cobalt ferrite with various compositions ($\text{Co}_x\text{Fe}_{3-x}\text{O}_4$, $x = 0.1$ (A), 0.3 (B), 0.5, 0.7 (C) and 1.0 (D)).

ferrites (Fig. 5A). Fig. 5B displays detailed deconvoluted XPS data of the C1 s core level peak. The peak consists of four components at binding energy of 285 eV (peak I), 287 eV (peak II), ~291 eV (peak III), which were assigned to C–C, C–O, and O–C=O bonds, respectively. These peaks were very intense in the $\text{Co}_{1.0}\text{Fe}_2\text{O}_4$ sample. The C1 s peak shape is characteristic of iron carbonate, FeCO_3 [50]. The C1 s peak is less intense in the other three samples of cobalt ferrites.

Fig. 5C shows the core level spectra of Fe2p doublet. The binding energy of Fe2p_{3/2} is at 710.2 eV of the $\text{Co}_{1.0}\text{Fe}_2\text{O}_4$ sample. As the cobalt content decreases, the binding energy increased, (e.g., 711.5 eV of the $\text{Co}_{0.1}\text{Fe}_{2.9}\text{O}_4$ sample). In the literature, the binding energy around 710.2 eV has been assigned to $\text{Co}_{1.0}\text{Fe}_2\text{O}_4$ [51] or iron carbonates FeCO_3 [50]. The binding energy ~711.5 eV is assigned to Fe^{3+} in Fe_2O_3 particles [52], probably in hematite ($\alpha\text{-Fe}_2\text{O}_3$) nanoparticles [53] or FeOOH [54]. By the asymmetry and the shape of 2p_{3/2} peak, we concluded that it is a sum of two contributions: at the low binding energy (cobalt ferrite, iron carbonate) and at the high binding energy (Fe_2O_3 or FeOOH). As the cobalt content decreases, the component at high binding energy is more intense in the whole spectrum, probably due to the absence of cobalt ferrite compounds on the surface. Finally, the O1s XP spectrum was not analyzed due to the presence of O1s component from the in substrate.

Fig. 5D shows the Co2p XP spectra, which suggest the shape and the binding energies are identical for the $\text{Co}_{1.0}\text{Fe}_2\text{O}_4$, $\text{Co}_{0.7}\text{Fe}_{2.3}\text{O}_4$, and

$\text{Co}_{0.5}\text{Fe}_{2.5}\text{O}_4$ samples. In the $\text{Co}_{0.1}\text{Fe}_{2.9}\text{O}_4$ sample, traces of Co appeared because of a small amount of Co atoms. The binding energy is at 780.0 eV, indicating that Co atoms are in cobalt ferrite bonds [51].

Using the total peak area of Co2p, Fe2p and O1s peaks (the contribution from the in substrate was subtracted), as well as the appropriate sensitivity factors (based on Wagner's collection and adjusted to the transmission characteristics of analyzer EA10) and the corresponding equations for the electron transport properties in the matrix [55] the % average relative atomic concentration in the analyzed region can be determined. The results are shown in Table 2.

3.2. Catalytic degradation and mineralization of $\text{Co}_x\text{Fe}_{3-x}\text{O}_4$

3.2.1. Role of $\text{Co}_x\text{Fe}_{3-x}\text{O}_4$ and PMS in PBSA degradation

The catalytic activities of the synthesized cobalt ferrite catalysts were evaluated for the degradation of PBSA in conjunction with PMS under various experimental conditions. Preliminary results of PBSA (initial concentration 4 μM) degradation by $\text{Co}_{0.7}\text{Fe}_{2.3}\text{O}_4$ (0.17 g/L) performed in the absence of PMS revealed no degradation in PBSA (Fig. 6). However, noticeable PBSA removal (i.e., 53%) at 240 min reaction time was observed upon addition of PMS to the previous system (Fig. 6, 1st use). Therefore, PMS was added to the reaction mixture as an oxidant for the degradation of PBSA. Moreover, experiments conducted in absence of light showed reasonable effectiveness in PBSA

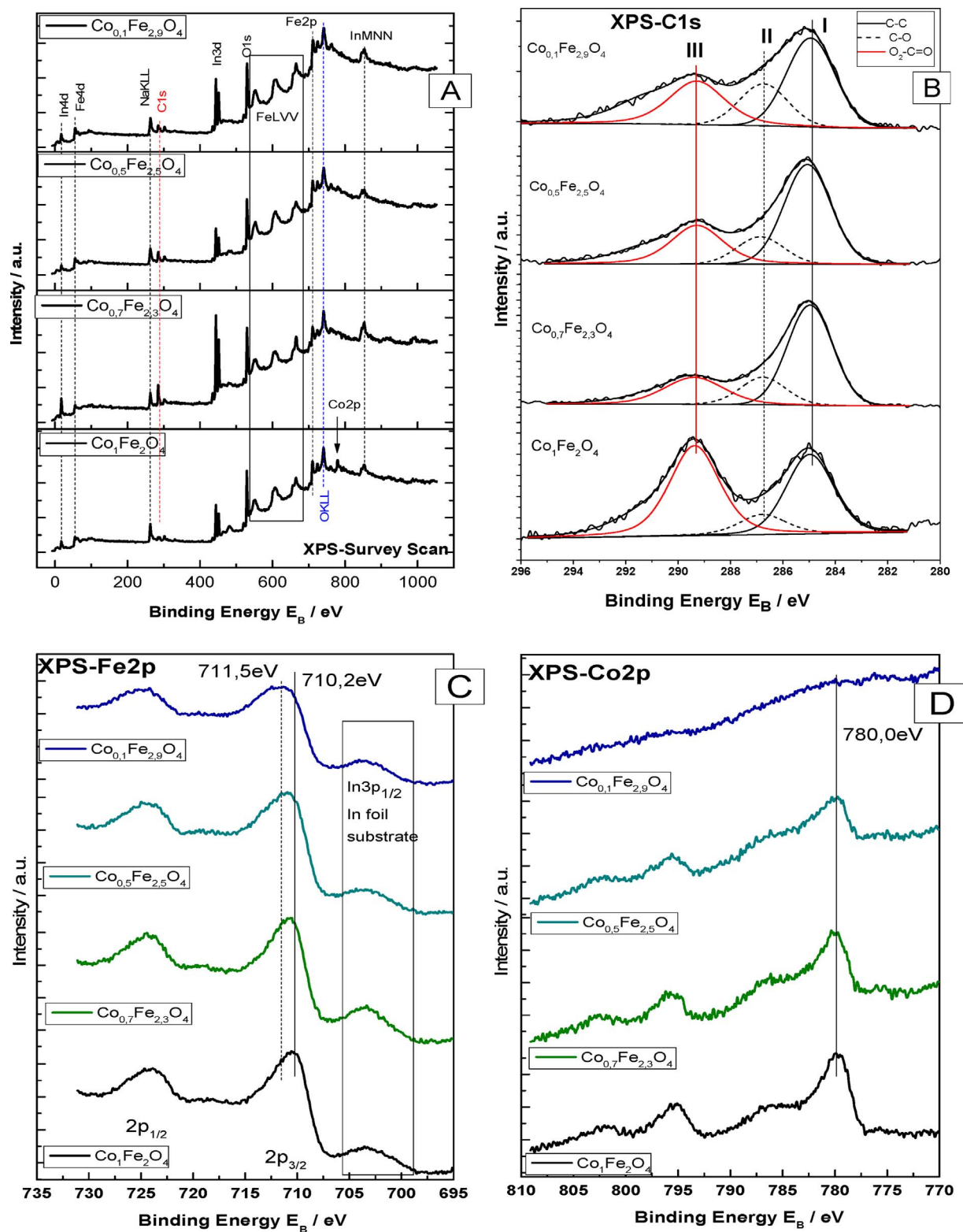


Fig. 5. (A) Survey scans from $\text{Co}_{0.1}\text{Fe}_{2.9}\text{O}_4$, $\text{Co}_{0.7}\text{Fe}_{2.3}\text{O}_4$, $\text{Co}_{0.5}\text{Fe}_{2.5}\text{O}_4$, and $\text{Co}_{0.1}\text{Fe}_{2.9}\text{O}_4$ samples on foil substrate; (B) Deconvoluted C1 s XP core level from $\text{Co}_{0.1}\text{Fe}_{2.9}\text{O}_4$, $\text{Co}_{0.7}\text{Fe}_{2.3}\text{O}_4$, $\text{Co}_{0.5}\text{Fe}_{2.5}\text{O}_4$, and $\text{Co}_{0.1}\text{Fe}_{2.9}\text{O}_4$ samples on indium foil substrate; (C) Fe2p XP core level from $\text{Co}_{0.1}\text{Fe}_{2.9}\text{O}_4$, $\text{Co}_{0.7}\text{Fe}_{2.3}\text{O}_4$, $\text{Co}_{0.5}\text{Fe}_{2.5}\text{O}_4$, and $\text{Co}_{0.1}\text{Fe}_{2.9}\text{O}_4$ samples on indium foil substrate; (D) Co2p XP core level from $\text{Co}_{0.1}\text{Fe}_{2.9}\text{O}_4$, $\text{Co}_{0.7}\text{Fe}_{2.3}\text{O}_4$, $\text{Co}_{0.5}\text{Fe}_{2.5}\text{O}_4$, and $\text{Co}_{0.1}\text{Fe}_{2.9}\text{O}_4$ samples on indium foil substrate.

Table 2

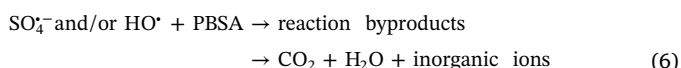
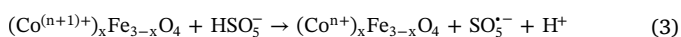
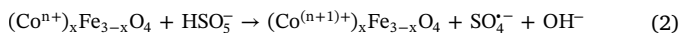
Surface relative atomic ratios derived from the XPS measurements.

sample	Co:Fe:O
Co _{1.0} Fe _{2.0} O ₄	1.0:2.1:5.1
Co _{0.7} Fe _{2.3} O ₄	0.7:2.5:5.4
Co _{0.5} Fe _{2.5} O ₄	0.5:2.8:6.4
Co _{0.1} Fe _{2.9} O ₄	(~0.1):3.2:6.0

(Experimental error: 10%).

removal which provides an energy-saving process for water treatment.

Previous studies suggested PMS is activated up on contact with cobalt metal ions [56,57] and cobalt-based ferrite nanoparticles (e.g., CoFe₂O₄) [58] and generate SO₄^{•−} and SO₅^{•−} species via Eq. (2) and (3). Reactive oxygen species (i.e., HO[•]) were also expected to generate in the system due to side reactions of sulfate radicals in the system per Eq. (4) and Eq. (5). The generated sulfate radical (Eq. (2) and Eq. (3)) [59], as well as hydroxyl radical (Eq. (4) and (5)) [60] were reported for their effectiveness as oxidants, and can effectively degrade PBSA according to Eq. (6).



Consequently, cobalt ions in the ferrite are the main factor in PMS activation in order to generate sulfate radicals and hydroxyl radicals, which are responsible for PBSA degradation. Therefore, it is predicted that Co:Fe stoichiometry, PMS concentration, and catalyst weight would have important roles on the overall degradation efficiency of PBSA, as will be discussed hereafter.

The degradation trend of PBSA in Co_{0.7}Fe_{2.3}O₄/PMS/PBSA in dark conditions was observed again in Fig. 6 using harvested, dried, and regenerated Co_{0.7}Fe_{2.3}O₄ from the prior experiments for a second (Fig. 6, 2nd reuse) and third reuse (Fig. 6, 3rd reuse). Surprisingly, PBSA degradation improved with each subsequent reuse of the catalyst, which could be due to activation of catalyst surface as it was continuously regenerated before each reuse (Section 2.3), or due to the increased surface area of the catalyst as a result of the additional sonication applied to the catalyst [61]. Possible leaching of cobalt ions from the catalysts was investigated in this study using ICP-MS. The

latter analysis revealed cobalt ion concentration was below the detection limit of 0.02 µg/L, eliminating possible contribution of leached ions on the degradation of PBSA. To be noted, a minor change in the pH of the reaction medium was noticed (i.e., from pH = 6.75 initially to 6.45), which may be due to the use of low initial PMS concentrations in the experiments. Therefore, all degradation and mineralization experiments were performed under uncontrolled pH conditions to avoid any possible buffer interference.

3.2.2. Effect of Co:Fe stoichiometry on PBSA degradation

Fig. 7A depicts the change in cobalt ferrite composition on PBSA degradation process in the presence of PMS. PBSA decomposed steeply using most of the prepared catalysts (i.e., x = 0.1, 0.7 and 1.0) within the first 15 min. This could be explained by the fast reaction between the Co-ferrite nanoparticles and PMS to generate SO₄^{•−} and HO[•] at the very initial phase of the mixing process. Afterwards, the decomposition rate of PBSA did not significantly change as the reaction time increased up to 240 min, which could be due to surface poisoning of the catalysts [62]. The current results revealed Co_{1.0}Fe_{2.0}O₄ to have the highest activation for PMS among all the prepared catalysts, indicating the superiority of cobalt over iron composition in the catalyst in PMS activation. For example, Co_{0.1}Fe_{2.9}O₄ had only 24% removal of PBSA in 240 min (Fig. 7A), at which Co_{1.0}Fe_{2.0}O₄ showed 75% removal of PBSA in the same reaction time. Intermediate removals of 55% and 70% in PBSA were obtained by Co_{0.5}Fe_{2.5}O₄ and Co_{0.7}Fe_{2.3}O₄ respectively, in 240 min reaction time. Analogous result of cobalt and iron behaviors was previously observed by Anipsitakis et al. in their study on the activation of PMS for the degradation of 2,4-dichlorophenol at near neutral pH values [63].

Even though Co_{1.0}Fe_{2.0}O₄ showed the optimum catalytic activity under the current experimental conditions, Co_{0.7}Fe_{2.3}O₄ was selected among the other prepared catalysts to examine the roles of catalyst loading and oxidant initial concentration. The selected catalyst was of moderate catalytic activity that allowed obtaining further insights on the maximum degradability of the pollutant under various experimental conditions.

3.2.3. Effect of catalyst loadings and PMS concentrations on PBSA degradation

Fig. 7B illustrates the effect of various PMS concentrations on PBSA degradation using Co_{0.7}Fe_{2.3}O₄ catalyst. It has been previously shown that the increased surface area of cobalt ferrite crystals leads to enhanced PBSA removal. The same effect was observed while increasing the PMS concentration. For example, at 60 min, increasing PMS concentration from 0.025 mM to 0.1 mM showed a steep increase in PBSA removal from 12 to 70% (Fig. 7B). However, further increase in PMS concentration up to 0.2 mM resulted in only 80% removal of PBSA.

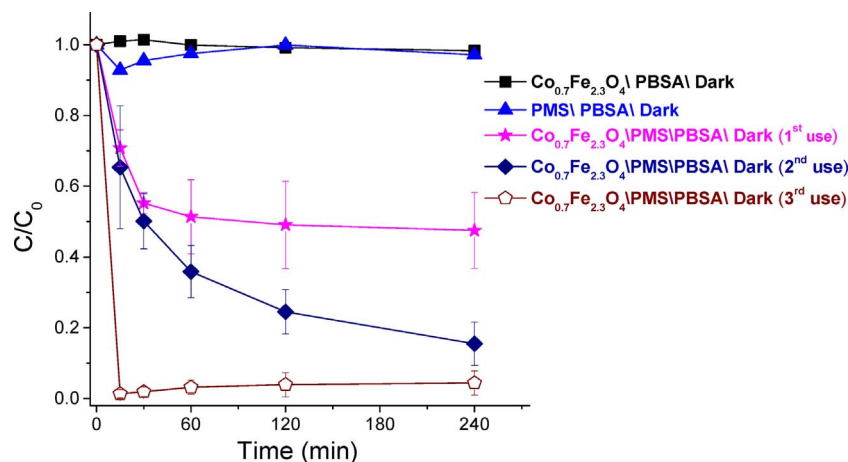


Fig. 6. Effect of PMS, Co_{0.7}Fe_{2.3}O₄ on PBSA degradation. Experimental conditions are: Co_{0.7}Fe_{2.3}O₄ = 0.17 g/L, [PMS]₀ = 0.1 mM, [PBSA]₀ = 4 µM.

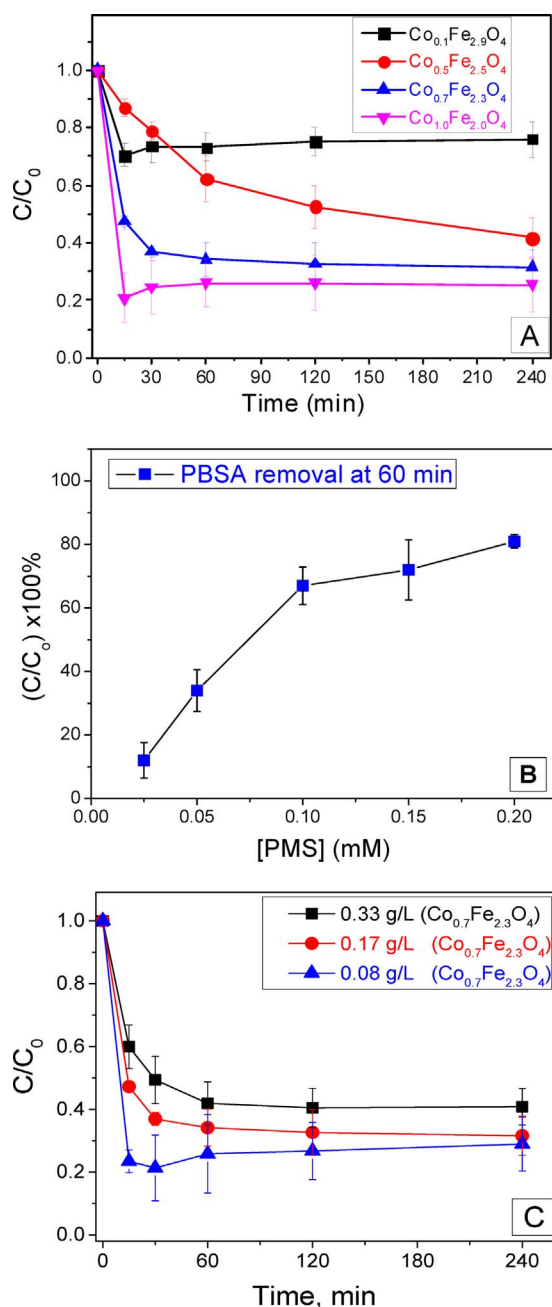


Fig. 7. (A) Effect of various stoichiometries of cobalt ferrite used in conjunction with PMS to remove PBSA from water samples over 240 min. Experimental conditions are: $Co_xFe_{3-x}O_4 = 0.17$ g/L, $[PMS]_0 = 0.1$ mM, $[PBSA]_0 = 4$ μ M. (B) PBSA removal percentage at 60 min reaction time at different PMS initial concentration. Experimental conditions are: $Co_{0.7}Fe_{2.3}O_4 = 0.17$ g/L (5 mg); $[PBSA]_0 = 4$ μ M. (C) Effect of catalyst ($Co_{0.7}Fe_{2.3}O_4$) weight (0.08, 0.17 and 0.33 g/L) on PBSA degradation. Experimental conditions are: $[PMS]_0 = 0.1$ mM, $[PBSA]_0 = 4$ μ M.

Generation of sulfate radicals and hydroxyl radicals would increase with the increase in PMS initial concentration, leading to a further enhanced removal of PBSA. However, a nonlinear PBSA removal, in respect to the linear increase in PMS concentration, was observed in the current study. This was most likely due to the scavenging effect, especially at higher oxidant concentrations (i.e., > 1.0 mM) [59,63].

Fig. 7C illustrates the effect of varying amounts of $Co_{0.7}Fe_{2.3}O_4$ on PBSA degradation over a 240 min reaction time. Three variations were attempted using 0.08, 0.17, and 0.33 g/L $Co_{0.7}Fe_{2.3}O_4$ in conjunction with fixed PMS and PBSA initial concentration, i.e., 0.1 mM and 4 μ M respectively. Using 0.33 g/L cobalt ferrite, 57% decrease in PBSA concentration was achieved in 240 min reaction. Interestingly, when the

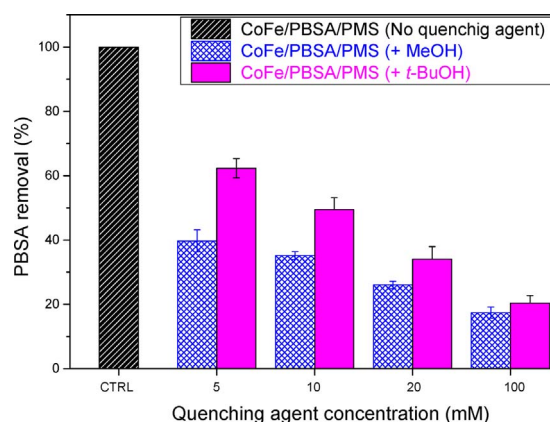


Fig. 8. Effect of different concentrations (5, 10, 20 and 100 mM) of quenching agents (MeOH and *t*-BuOH) on the (A) overall degradation of PBSA and (B) PBSA removal percentage at 240 min. Experimental conditions are: $Co_{1.0}Fe_{2.0}O_4 = 0.17$ g/L, $[PMS]_0 = 0.1$ mM, $[PBSA]_0 = 4$ μ M.

catalyst dose decreased to 0.17 and 0.08 g/L, the PBSA removal increased to 70 and 72%, respectively. It was hypothesized that at higher catalyst dose (e.g., 0.33 and 0.17 g/L), magnetic nanoparticles showed a clumping effect, that resulted in a loss of surface area and ultimately less reactivity towards PMS and decreased PBSA degradation.

3.2.4. HO^\bullet and $SO_4^{\bullet-}$ contribution to PBSA degradation

To establish a pathway for PBSA degradation process, identification of the reactive radical species (i.e., HO^\bullet and $SO_4^{\bullet-}$) in the system is required. For this purpose, a chemical probe method was utilized in this study. In the experiment, alcohols with (MeOH) and without (*t*-BuOH) α -hydrogen were used as free radical scavengers during the reaction [64–66]. In this experiment, MeOH was hypothesized to quench HO^\bullet (i.e., $k_{MeOH,HO^\bullet} = 9.7 \times 10^8$ $M^{-1}s^{-1}$) and $SO_4^{\bullet-}$ (i.e., $k_{MeOH,SO_4^{\bullet-}} = 1.0 \times 10^7$ $M^{-1}s^{-1}$) at similar extent, while *t*-BuOH could quench HO^\bullet (i.e., $k_{t-BuOH,HO^\bullet} = 3.8\text{--}7.6 \times 10^8$ $M^{-1}s^{-1}$) at 10^3 times faster than $SO_4^{\bullet-}$ (i.e., $k_{t-BuOH,SO_4^{\bullet-}} = 4 \times 10^5$ – 9.1×10^5 $M^{-1}s^{-1}$) [66].

The results of PBSA degradation by cobalt ferrite-PMS system in presence of different MeOH and *t*-BuOH concentrations (i.e., 5, 10, 20 and 100 mM) are shown in Fig. 8. The results suggested both $SO_4^{\bullet-}$ and HO^\bullet were involved in the degradation process, with hydroxyl radical dominating over sulfate radicals. Moreover, $SO_4^{\bullet-}/HO^\bullet$ ratio was suggested to increase in the solution at longer degradation times due to release of H^+ during PMS hydrolysis. This is consistent with the previous finding by Zhang et al. who observed the contribution of both $SO_4^{\bullet-}$ and HO^\bullet in the degradation of PBSA by PMS in presence of $CuFe_2O_4$ as a catalyst [29].

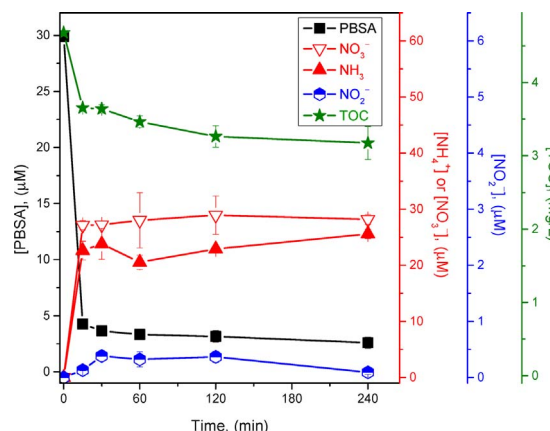


Fig. 9. Formation of NO_2^- , NO_3^- and NH_4^+ during the catalytic degradation of PBSA. Experimental conditions are: $Co_{1.0}Fe_{2.0}O_4 = 0.17$ g/L, $[PMS]_0 = 0.6$ mM, $[PBSA]_0 = 30$ μ M.

3.3. Mineralization of PBSA

Mineral residues were expected to generate during, and at the end, of PBSA degradation by $\text{Co}_x\text{Fe}_{3-x}\text{O}_4/\text{PMS}$ due to presence of C, S and N atoms in PBSA chemical structure. Reduction in the total organic carbon (TOC) content of the PBSA degradation system was also expected as a result of the complete oxidation of PBSA and its degradation byproducts. Fig. 9 reveals the concentration profile of released NO_2^- , NO_3^- and NH_4^+ during the degradation process. The formation of NH_4^+ and NO_3^- (as explained in Section 3.4.2.4) was exceptionally rapid with their respective maximum release of 23.8 and 27.2 μM achieved in 15 min, when 87% of PBSA was removed effectively. Longer reaction times (> 15 min) did not exhibit any significant change in the concentration level of the both NH_4^+ and NO_3^- or the parent compound PBSA. Overall, formation of NO_2^- was marginal during the degradation process as compared to other forms of inorganic nitrogen detected in the same system. The nature of NO_2^- under the operated experimental conditions was explained via its slow and low release (i.e., 0.38 μM) in the first 30 min of the reaction (see next section). In support of the last finding, previous studies reported the ease of nitrite ions oxidation into nitrate species, especially in oxidative systems [19,67]. It is also possible for $-\text{SO}_3\text{H}$ moiety in PBSA to be released in the form of sulfate ions (i.e., SO_4^{2-}) [19–21], as further confirmed by LC/Q-TOF-ESI-MS results in the present study. However, due to SO_4^{2-} released from PMS hydrolysis, SO_4^{2-} transformed from PBSA during the degradation process could not be accurately measured (data are not shown).

Fig. 9 shows the result of TOC reduction in the Fe-Co/PMS/PBSA degradation system. Only 32% of the theoretical total TOC was reduced after 240 min of the reaction, and most of TOC (about 22%) was removed within the first 15 min of the reaction. This indicated the possibility of complete mineralization of PBSA by the current degradation system, which requires longer degradation time.

3.4. Degradation byproducts and pathways of PBSA

3.4.1. Degradation byproducts

Detailed transformation byproducts of PBSA by $\text{Co}_{1.0}\text{Fe}_{2.0}\text{O}_4$ activated PMS were identified and reaction pathways were suggested. Identification of the byproducts was accomplished by analyses of extracted ion chromatogram (i.e., peak area), retention time (R_t), suggested formula and m/z values given by the analytical software [68]. To maximize the efficiency of byproducts detection by the current

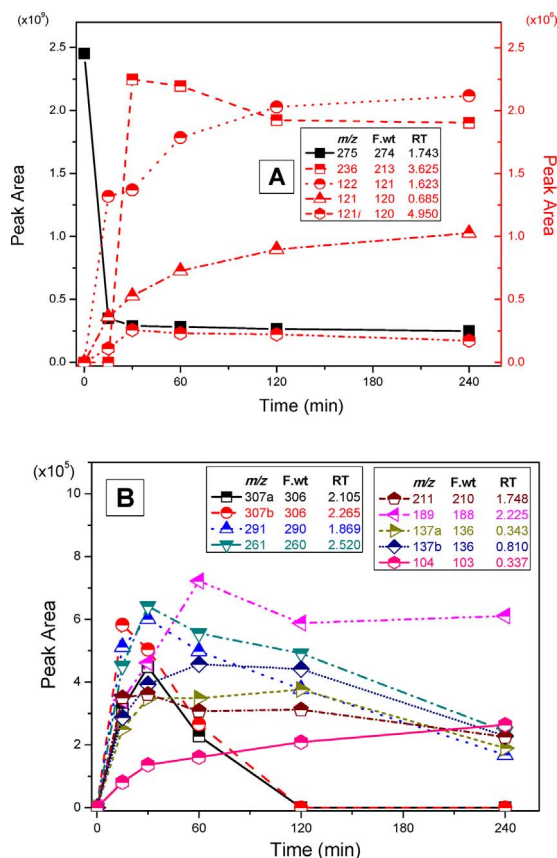


Fig. 10. Degradation of PBSA and the release of byproducts using LC/Q-TOF-ESI-MS. Experimental conditions are: $\text{Co}_{1.0}\text{Fe}_{2.0}\text{O}_4 = 0.17$ g/L, $[\text{PMS}]_0 = 0.6$ mM, $[\text{PBSA}]_0 = 30$ μM .

experimental method, a high initial concentration PBSA (i.e. 30 μM) was employed in the degradation system. The formulae of major reaction byproducts generated during a reaction period of 240 min were identified and recorded in Table 3. With the presented experimental conditions and analytical techniques, 15 byproducts were detected, including mono-(PBSA-OH, m/z 291), di-(PBSA-2OH, m/z 307) and tri-hydroxylated PBSA (PBSA-3OH, m/z 323); mono-hydroxylated phenylbenzimidazole (PBI-OH, m/z 211); aldehyde (CBX-1, m/z 177) and

Table 3

LC/Q-TOF-ESI-MS results collected during the catalytic degradation of PBSA: measurement of chromatogram peak area corresponding to each byproduct at each time interval according to their suggested molecular weight (MW), formula, m/z , and retention time (RT). Experimental conditions are weight of $\text{Co}_{1.0}\text{Fe}_{2.0}\text{O}_4 = 0.17$ g/L, $[\text{PMS}]_0 = 0.6$ mM, $[\text{PBSA}]_0 = 30$ μM .

Formula	Short name	m/z	MW	RT (min)	Reaction time (min)					
					0	15	30	60	120	240
$\text{C}_{13}\text{H}_{10}\text{N}_2\text{O}_6\text{S}$	PBSA-3OH	323	322	1.561	0	0	0	0	158649	0
$\text{C}_{13}\text{H}_{10}\text{N}_2\text{O}_5\text{S}-1^+$	PBSA-2OH	307a	306	2.105	0	316973	448552	228357	0	0
$\text{C}_{13}\text{H}_{10}\text{N}_2\text{O}_5\text{S}-2^+$	PBSA-2OH	307b	306	2.265	0	582373	503924	265688	0	0
$\text{C}_{13}\text{H}_{10}\text{N}_2\text{O}_4\text{S}$	PBSA-OH	291	290	1.869	0	512577	601622	498499	378044	168231
$\text{C}_{13}\text{H}_{10}\text{N}_2\text{O}_3\text{S}$	PBSA	275	274	1.743	2452679000	350318686	288971904	28273299	266033760	249504208
$\text{C}_{13}\text{H}_{12}\text{N}_2\text{O}_4$	BCIA	261	260	2.52	0	452004	641643	555767	491814	243351
$\text{C}_{13}\text{H}_{11}\text{NO}_2$	HP-BD	236	213	3.625	0	0	22471498	21971594	19255618	19042416
$\text{C}_{11}\text{H}_8\text{N}_2\text{O}_3$	CBX-1	217	216	2.092	0	99294	0	0	0	0
$\text{C}_{13}\text{H}_{10}\text{N}_2\text{O}$	PBI-OH	211	210	1.748	0	351132	361352	307954	312276	225340
$\text{C}_{10}\text{H}_8\text{N}_2\text{O}_2$	CBX-2	189	188	2.225	0	342927	461464	721853	588013	610540
$\text{C}_7\text{H}_8\text{N}_2\text{O}-1^+$	BZD-OH	137a	136	0.343	0	250041	348016	348583	376609	189561
$\text{C}_7\text{H}_8\text{N}_2\text{O}-2^+$	BZD-OH	137b	136	0.81	0	287408	393017	457042	441451	228202
$\text{C}_7\text{H}_7\text{NO}$	BD	122	121	1.623	0	13184431	13706640	17865202	20301770	21196106
$\text{C}_7\text{H}_8\text{N}_2$	BZD	121	120	0.685	0	3626146	5270510	7267994	8976447	10271960
$\text{C}_7\text{H}_4\text{O}_2$	4-OMCD	121i	120	4.95	0	1108978	2571801	2310323	2227322	1718611
$\text{C}_7\text{H}_5\text{N}$	Benzonitrile (BNT)	104	103	0.337	0	81057	136357	160885	209024	264042

* Compounds assigned with (1) and (2) represent possible isomers of the same formula.

carboxyl (CBX-2, m/z 189) derivatives of phenylimidazole; imidazole ring opening with the formation of *N*'-hydroxy-*N*-(hydroxyphenyl) benzenecarboximidamide (BCIA, m/z 261), hydroxyphenyl benzamide (HP-BD m/z 236), benzamide (BD, m/z 121) and benzimidine (BZD, m/z 122), mono-hydroxylated derivative of BZD (BZD-OH, m/z 137) in addition to other BD and BZD derivatives namely, benzonitrile (BNT, m/z 104) and 4-(oxomethylidene)cyclohexa-2,5-dien-1-one (4-OMCD, m/z 121i). Interestingly, the compounds BCIA, HP-BD, BNT and 4-OMCD were newly detected by the analysis method used in this study.

Fig. 10(A) and (B) depicts the kinetics profile (i.e., in terms of change in peak area) of PBSA and its byproducts during the degradation experiments. According to Fig. 10(A), nearly 65% PBSA was effectively removed by $\text{Co}_{1.0}\text{Fe}_{2.0}\text{O}_4/\text{PMS}$ system in 120 min of reaction time. In parallel to that, the formation of byproducts, and their further degradation, varied from one to another in terms of their peak areas (Fig. 10(A) and (B)). Among the 15 byproducts detected, only four of them (HP-BD (m/z 236), BD (m/z 122), BZD (m/z 121) and 4-OMCD (m/z 121i)) showed the highest abundance, as represented by their peak areas. Generally, all the recognized byproducts evolved progressively in the solution during the first 30 – 60 min of the degradation process; however, various evolution profiles were noticed at extended reaction period. For example, after 30 min, the compounds BZD, BD and BNT continued liberating into the solution but with much slower rates. The BD and BZD byproducts were previously detected during the degradation of PBSA by different technologies, UV/ H_2O_2 [21], UV/ TiO_2 [20] and $\text{CuFe}_2\text{O}_4/\text{PMS}$ [29], which is consistent with the current results. The di-hydroxylated PBSA isomers (PBSA-2OH, m/z 307a and 307b) exhibited exceptionally fast degradation rate (at time > 30 min), with their complete removal reached within 2 h of reaction. Slower removals of BCIA (m/z 261), PBSA-OH (m/z 291), PBI (m/z 211) and the two BZD-OH isomers (137a and 137b) were observed over time, with only 38, 28, 26 and 50% reduction in their respective maximum peak area achieved in 240 min (Fig. 10B). The remaining byproducts (i.e., CBX-2, m/z 189; HP-BD, 236; 4-OMCD 121i) revealed steady release profile over time, which implied their comparable removal and release rates during 2 h reaction time span. The formation of tri-hydroxylated byproduct of PBSA (PBSA-3OH, m/z 323) and CBX-1 (m/z 217) were previously detected during the degradation of PBSA by UV/ TiO_2 [20] and UV/ H_2O_2 [21], respectively. However, in the current study, PBSA-3OH and CBX-1 were only detected at 15 and 120 min, respectively, and then disappeared from the solution (Table 3), suggesting their low chemical stability/fast degradation under the current experimental conditions. Unexpectedly, phenylbenzimidazole (PBI, m/z 195), was not found among the pool of identified byproducts, yet the existence of monohydroxylated derivative of PBI (i.e., PBI-OH, m/z 211) proved the formation of PBI. The last compound was previously reported by Ji et al. (2013) as one of the byproducts from the photocatalytic degradation of PBSA by TiO_2 [20], which may reflect the low sensitivity of currently employed analytical method towards the detection of PBI.

3.4.2. Degradation pathways

The potential pathways of PBSA degradation are presented in Scheme 1. Hydroxylation of PBSA, removal of sulfonate moiety, and ring cleavage were recognized as the main degradation pathways.

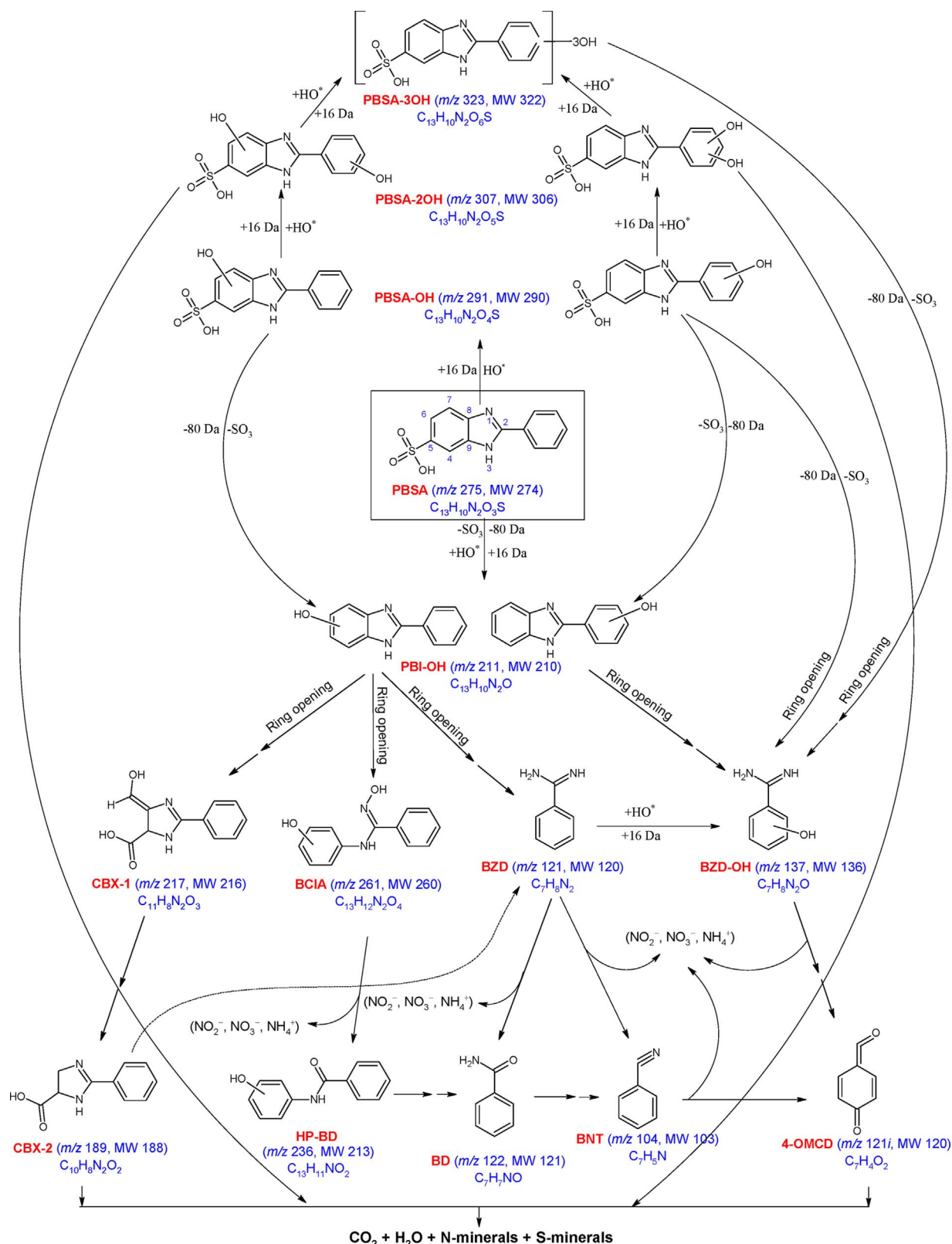
3.4.2.1. Hydroxylation byproducts of PBSA. Introducing hydroxyl groups (–OH) onto the two benzene rings of PBSA could take place via either $\text{SO}_4^{\cdot-}$ or HO^{\cdot} attack to a carbon atom containing α -Hydrogen [21,29,69]. Schemes 2 and 3 illustrate mechanisms of a PBSA hydroxylation process by HO^{\cdot} and $\text{SO}_4^{\cdot-}$, respectively. In typical HO^{\cdot} attack, a carbon-centered radical is produced upon electrophilic addition of HO^{\cdot} to PBSA benzene ring (Scheme 2). The resulting organic radical readily reacts with dissolved O_2 to form a thermally unstable peroxy radical, which tends to form monohydroxylated PBSA byproduct (i.e., PBSA-OH) after releasing the hydroperoxy radical ($\text{H}_2\text{O}^{\cdot}$) [69]. In case of $\text{SO}_4^{\cdot-}$ attack, a cationic benzene radical is generated which hydrolyzes directly (in aqueous medium) to form a

carbon-centered radical. Like the HO^{\cdot} -mediated mechanism, the generated organic radical reacts with O_2 to form an organic peroxy radical that converts into PBSA-OH after HOO^{\cdot} release. With the progressive attacks of HO^{\cdot} and $\text{SO}_4^{\cdot-}$ to PBSA, highly hydroxylated byproducts (i.e., PBSA-2OH and PBSA-3OH) are produced [20,21,29]. Actually, there are different available attack sites on the aromatic rings of PBSA, however, their susceptibility towards HO^{\cdot} and $\text{SO}_4^{\cdot-}$ is influenced by different factors, including steric hindrance and presence of electron withdrawing groups and resonance stability. Arbitrary attachment of –OH group(s) to the two benzene rings of PBSA was suggested in Scheme 1.

3.4.2.2. Elimination of sulfonate moiety. Stability of sulfonate moiety on PBSA at room temperature is linked with its electron-withdrawing nature [21]. However, several photochemical and photocatalytic degradations studies reported the release of sulfonate group from PBSA in the form of SO_4^{2-} [21,29]. Direct monitoring of released SO_4^{2-} by Ion chromatographic (IC) technique was difficult in the current study, yet, the results of LC/Q-TOF-ESI-MS confirmed this hypothesis via formation of sulfonate-free-byproducts. For example, the formation of PBI-OH (m/z 210) by direct radical attack to C5 or C6 of PBSA, or by the release of SO_4^{2-} from PBSA-OH. Similar observations were reported in previous studies established on the degradation of PBSA by UV/ H_2O_2 [19,21], TiO_2/UV [20], and Cu-Fe/PMS [29].

3.4.2.3. Radical attack at benzimidazole rings of PBSA. Due to the high electron density on benzimidazole rings of PBSA, they are progressively attacked by both HO^{\cdot} and $\text{SO}_4^{\cdot-}$ to generate a pool of hydroxylated byproducts including PBI-OH [20,21]. With the continuous oxidation, bonds of PBI-OH start to cleavage with ultimate ring opening to form the first carboxylic acid in the degradation system (CBX-1), and BZD and its derivative byproducts BCIA and BZD-OH. The formation of BZD-OH was also suggested via hydroxylation of BZD by a mechanism similar to those shown in Schemes 2 and 3, or the by the release of SO_4^{2-} followed by benzimidazole ring opening of PBSA-OH and PBSA-3OH [20,21]. The formation of CBX-1 and its further degradation into CBX-2 was previously explained to occur via consecutive oxidation of the aldehyde group of CBX-1 followed by loss of CO_2 (i.e., –44 Da) [21]. BZD could also be generated from CBX-1 through consecutive radical attacks to its imidazole ring.

3.4.2.4. Release of NO_2^- , NO_3^- and NH_4^+ . The formation of NO_2^- , NO_3^- and NH_4^+ during PBSA degradation was justified as the BCIA, BZD and BZD-OH compounds lost one or two N-atoms due to attack by the hydroxyl and sulfate radicals in the medium. Similar release of NH_4^+ and NO_3^- was previously reported during the degradation of PBSA by UV/ H_2O_2 and UV/ TiO_2 technologies [19,20]. Moreover, Abdelraheem et al. (2015) revealed the possible oxidation of ammonia into nitrate ions during AOPs, especially in the presence of powerful catalysts such as TiO_2 [21]. Nitrite ions were also detected in the current study at considerably low concentrations as compared to nitrate and ammonia. This was rationalized as the cobalt ferrite catalyst promoted the release of organic N-atoms initially in the form of NO_2^- , which is then oxidized into NO_3^- at the catalyst surface. Overall, about 90% of nitrogen content in PBSA was majorly converted into NO_3^- and NH_4^+ ions, and marginally into NO_2^- in 240 min reaction time in the current study. This was consistent with the current LC-MS results, where less nitrogen-containing byproducts (e.g., BNT and 4-OMCD) were obtained at prolonged degradation times. Analogous observation of NO_3^- release with the formation of N-free compound (4-OMCD) was also noticed by Song et al. during the degradation of *p*-nitrotoluene (i.e., a nitrogen containing compound) by $\text{O}_3/\text{sonolysis}$ AOP [70]. Overall, cobalt ferrite successfully activated PMS to generate sulfate radical and reactive oxygen species for the degradation of PBSA.

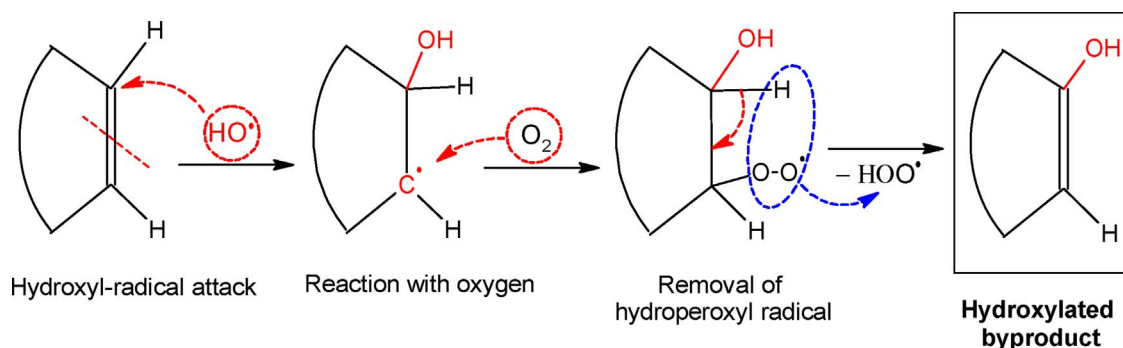
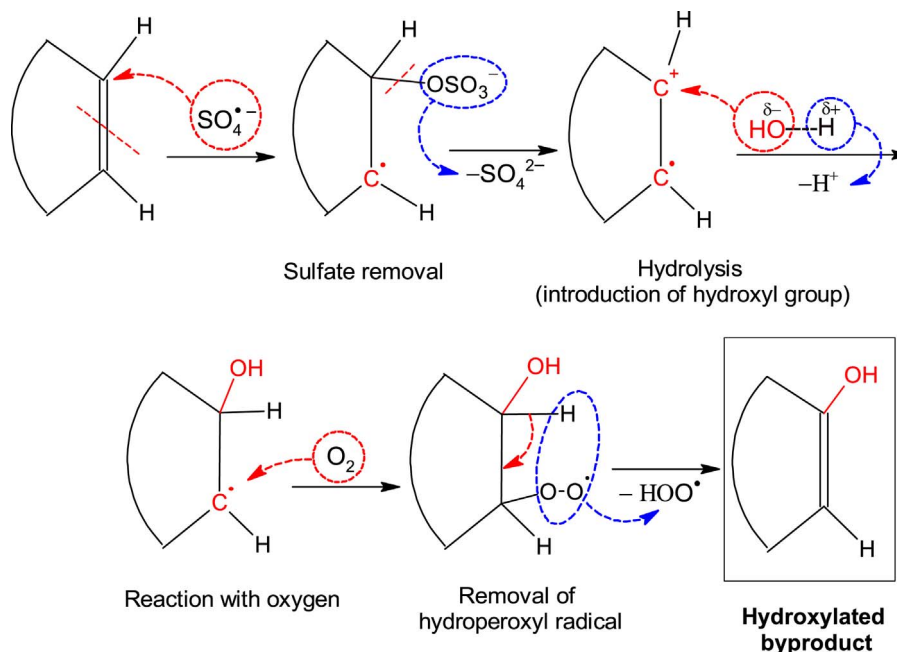


Scheme 1. Suggested degradation pathways of PBSA by $Co_{1.0}Fe_{2.0}O_4$ /PMS system. Experimental conditions: weight of $Co_{1.0}Fe_{2.0}O_4$ = 5 mg, $[PMS]_0$ = 0.6 mM, $[PBSA]_0$ = 30 μ M.

4. Conclusion

The presented work provided a deeper insight into the fabrication of spinel $Co_xFe_{3-x}O_4$ nanoparticles via the combustion synthesis method as well as their use as catalysts for the treatment of wastewater. The synthesized magnetic nanoparticles demonstrated interesting and

useful behavior when used in conjunction with PMS for the degradation of PBSA in water. Studies on the role of various Co:Fe stoichiometry showed $Co_{1.0}Fe_{2.0}O_4$ is the most effective by removing ~75% PBSA in 240 min of reaction time in the presence of 0.1 mM PMS. The effect of initial concentrations of PMS on PBSA degradation was also studied and 0.1 mM PMS shown the optimal PBSA degradation. The magnetic

Scheme 2. Mechanism of PBSA attack by $\text{HO}\cdot$ with the formation of hydroxylated byproducts.Scheme 3. Mechanism of PBSA attack by $\text{SO}_4^{\cdot-}$ with the formation of hydroxylated byproducts.

nanoparticles showed a promising reusability behavior as they interestingly showed increasing catalytic performance with each subsequent use. Both sulfate radical and hydroxyl radical appeared to contribute to PBSA degradation. Mineralization of PBSA was majorly in the form of nitrate and ammonium ions with minor formation of nitrite ions. Moreover, only 32% reduction in TOC was obtained at 240 min of reaction time. Fifteen byproducts from PBSA degradation were identified using LC/MS analysis. Degradation pathways of PBSA were also suggested based on the detected byproducts. Overall, $\text{Co}_x\text{Fe}_{3-x}\text{O}_4$ was shown to be a promising magnetic catalyst for water treatment due to its easy removal as well as the possibility of its subsequent reuse while maintaining its catalytic performance.

Acknowledgements

The authors gratefully acknowledge the support from the Kingdom of Saudi Arabia, ministry of higher education for providing King Abdullah scholarship to AA. P.F. also acknowledges funding by Prince Sultan Bin Abdulaziz International Prize for Water (PSIPW)-Alternative Water Resources Prize 2014.

Appendix A. Supplementary data

Supplementary data associated with this article can be found, in the online version, at <http://dx.doi.org/10.1016/j.apcatb.2017.08.054>.

References

- [1] X. Duan, H. Sun, J. Kang, Y. Wang, S. Indrawirawan, S. Wang, Insights into heterogeneous catalysis of persulfate activation on dimensional-structured nanocarbons, *ACS Catal.* 5 (2015) 4629–4636.
- [2] S. Shylesh, V. Schünemann, W.R. Thiel, Magnetically separable nanocatalysts: bridges between homogeneous and heterogeneous catalysis, *Angew. Chem. Int. Ed.* 49 (2010) 3428–3459.
- [3] V. Polshettiwar, R.S. Varma, Nanoparticle-supported and magnetically recoverable Ruthenium hydroxide catalyst: efficient hydration of nitriles to Amides in aqueous medium, *Chemistry* 15 (2009) 1582–1586.
- [4] A.H. Lu, E.L. Salabas, F. Schüth, Magnetic nanoparticles: synthesis, protection, functionalization, and application, *Angew. Chem. Int. Ed.* 46 (2007) 1222–1244.
- [5] Z. Iatridi, K. Vamvakidis, I. Tsougos, K. Vassiou, C. Dendrinou-Samara, G. Bokias, Multifunctional polymeric platform of magnetic ferrite colloidal superparticles for luminescence, imaging, and hyperthermia applications, *ACS Appl. Mater. Interfaces* 8 (2016) 35059–35070.
- [6] Q. Dai, K. Patel, G. Donatelli, S. Ren, Magnetic cobalt ferrite nanocrystals for an energy storage concentration cell, *Angew. Chem. Int. Ed.* 55 (2016) 10439–10443.
- [7] N. Sharma, H. Ojha, A. Bharadwaj, D.P. Pathak, R.K. Sharma, Preparation and catalytic applications of nanomaterials: a review, *RSC Adv.* 5 (2015) 53381–53403.
- [8] X. Wu, W. Wang, F. Li, S. Khaimanov, N. Tsiadaeva, M. Lahoubi, PEG-assisted hydrothermal synthesis of CoFe_2O_4 nanoparticles with enhanced selective adsorption properties for different dyes, *Appl. Surf. Sci.* 389 (2016) 1003–1011.
- [9] Y. Hou, X. Li, Q. Zhao, G. Chen, ZnFe_2O_4 multi-porous microbricks/graphene hybrid photocatalyst: facile synthesis, improved activity and photocatalytic mechanism, *Appl. Catal. B: Environ.* (2013) 80–88.
- [10] D.H.K. Reddy, Y.-S. Yun, Spinel ferrite magnetic adsorbents: alternative future materials for water purification? *Coord. Chem. Rev.* 315 (2016) 90–111.
- [11] E. Casbeer, V.K. Sharma, X.-Z. Li, Synthesis and photocatalytic activity of ferrites under visible light: a review, *Sep. Purif. Technol.* 87 (2012) 1–14.
- [12] M. Su, C. He, V.K. Sharma, M.A. Asi, D. Xia, X.-z. Li, H. Deng, Y. Xiong, Mesoporous

- zinc ferrite: synthesis, characterization, and photocatalytic activity with H_2O_2 /visible light, *J. Hazard. Mater.* 211 (2012) 95–103.
- [13] L.T. Lu, N.T. Dung, L.D. Tung, C.T. Thanh, O.K. Quy, N.V. Chuc, S. Maenosono, N.T. Thanh, Synthesis of magnetic cobalt ferrite nanoparticles with controlled morphology, monodispersity and composition: the influence of solvent, surfactant, reductant and synthetic conditions, *Nanoscale* 7 (2015) 19596–19610.
 - [14] V. Kashyap, S.K. Singh, S. Kurungot, Cobalt ferrite bearing nitrogen-doped reduced graphene oxide layers spatially separated with microporous carbon as efficient oxygen reduction electrocatalyst, *ACS Appl. Mater. Interfaces* 8 (2016) 20730–20740.
 - [15] Y. Fu, H. Chen, X. Sun, X. Wang, Combination of cobalt ferrite and graphene: high-performance and recyclable visible-light photocatalysis, *Appl. Catal. B: Environ.* 111–112 (2012) 280–287.
 - [16] P. Hu, M. Long, Cobalt-catalyzed sulfate radical-based advanced oxidation: a review on heterogeneous catalysts and applications, *Appl. Catal. B: Environ.* 181 (2016) 103–117.
 - [17] E. Manova, G. von, Organic UV filters in personal care products in Switzerland: a survey of occurrence and concentrations, *Int. J. Hyg. Environ. Health* 216 (2013) 508.
 - [18] A. Wick, G. Fink, T.A. Ternes, Comparison of electrospray ionization and atmospheric pressure chemical ionization for multi-residue analysis of biocides, UV-filters and benzothiazoles in aqueous matrices and activated sludge by liquid chromatography-tandem mass spectrometry, *J. Chromatogr. A* 1217 (2010) 2088–2103.
 - [19] W.H.M. Abdelraheem, X. He, X. Duan, D.D. Dionysiou, Degradation and mineralization of organic UV absorber compound 2-phenylbenzimidazole-5-sulfonic acid (PBSA) using UV-254 nm/ H_2O_2 , *J. Hazard. Mater.* 282 (2015) 233–240.
 - [20] Y. Ji, L. Zhou, C. Ferronato, A. Salvador, X. Yang, J.-M. Chovelon, Degradation of sunscreen agent 2-phenylbenzimidazole-5-sulfonic acid by TiO_2 photocatalysis: kinetics, photoproducts and comparison to structurally related compounds, *Appl. Catal. B: Environ.* 140–141 (2013) 457–467.
 - [21] W.H.M. Abdelraheem, X. He, Z.R. Komy, N.M. Ismail, D.D. Dionysiou, Revealing the mechanism, pathways and kinetics of UV_{254nm}/ H_2O_2 -based degradation of model active sunscreen ingredient PBSA, *Chem. Eng. J.* 288 (2016) 824–833.
 - [22] B.-T. Zhang, Y. Zhang, Y. Teng, M. Fan, Sulfate radical and its application in decontamination technologies, *Crit. Rev. Environ. Sci. Technol.* 45 (2015) 1756–1800.
 - [23] C. Jiang, Y. Ji, Y. Shi, J. Chen, T. Cai, Sulfate radical-based oxidation of fluoroquinolone antibiotics: kinetics, mechanisms and effects of natural water matrices, *Water Res.* 106 (2016) 507–517.
 - [24] M. Feng, L. Gizmas, Z. Wang, V.K. Sharma, Synergistic effect of aqueous removal of fluoroquinolones by a combined use of peroxymonosulfate and ferrate(VI), *Chemosphere* 177 (2017) 144–148.
 - [25] R.E. Huie, C.L. Clifton, P. Neta, Electron transfer reaction rates and equilibria of the carbonate and sulfate radical anions: international, *Int. J. Radiat. Appl. Instrum. C Radiat. Phys. Chem.* 38 (1991) 477–481.
 - [26] W.-D. Oh, Z. Dong, T.-T. Lim, Generation of sulfate radical through heterogeneous catalysis for organic contaminants removal: current development, challenges and prospects, *Appl. Catal. B: Environ.* 194 (2016) 169–201.
 - [27] Y. Feng, D. Wu, Y. Deng, T. Zhang, K. Shih, Sulfate radical-Mediated degradation of sulfadiazine by CuFeO_2 rhombohedral crystal-catalyzed peroxymonosulfate: synergistic effects and mechanisms, *Environ. Sci. Technol.* 50 (2016) 3119–3127.
 - [28] R. Jiang, H.Y. Zhu, J.B. Li, F.Q. Fu, J. Yao, S.T. Jiang, G.M. Zeng, Fabrication of novel magnetically separable $\text{BiOBr}/\text{CoFe}_2\text{O}_4$ microspheres and its application in the efficient removal of dye from aqueous phase by an environment-friendly and economical approach, *Appl. Surf. Sci.* 364 (2016) 604–612.
 - [29] X. Zhang, M. Feng, L. Wang, R. Qu, Z. Wang, Catalytic degradation of 2-phenylbenzimidazole-5-sulfonic acid by peroxymonosulfate activated with nitrogen and sulfur co-doped CNTs-COOH loaded CuFe_2O_4 , *Chem. Eng. J.* 307 (2017) 95–104.
 - [30] P.P. Swamy, S. Basavaraja, A. Lagashetty, N.S. Rao, R. Nijaganappa, A. Venkataraman, Synthesis and characterization of zinc ferrite nanoparticles obtained by self-propagating low-temperature combustion method, *Bull. Mater. Sci.* 34 (2011) 1325–1330.
 - [31] T. Striker, J.A. Ruud, Effect of fuel choice on the aqueous combustion synthesis of lanthanum ferrite and lanthanum manganite, *J. Am. Ceram. Soc.* 93 (2010) 2622–2629.
 - [32] B. Parvatheeswara Rao, G. Rao, A. Mahesh Kumar, K. Rao, Y. Murthy, S. Hong, C.-O. Kim, C. Kim, Soft chemical synthesis and characterization of $\text{Ni}_{0.65}\text{Zn}_{0.35}\text{Fe}_2\text{O}_4$ nanoparticles, *J. Appl. Phys.* 101 (2007) 123902.
 - [33] E. Chiellini, A. Corti, S. D'Antone, R. Solaro, Biodegradation of poly (vinyl alcohol) based materials, *Prog. Polym. Sci.* 28 (2003) 963–1014.
 - [34] M. Sajjia, T. Oubaha, A.G. Prescott, Development of cobalt ferrite powder preparation employing the sol/gel technique and its structural characterization, *J. Alloys Compd.* 506 (2010) 400–406.
 - [35] A. Cabanas, M. Poliakoff, The continuous hydrothermal synthesis of nano-particulate ferrites in near critical and supercritical water, *J. Mater. Chem.* 11 (2001) 1408–1416.
 - [36] T. Itoh, Y. Nishida, A. Tomita, Y. Fujie, Determination of the crystal structure and charge density of $(\text{Ba}_{0.5}\text{Sr}_{0.5})(\text{Co}_{0.8}\text{Fe}_{0.2})\text{O}_{2.33}$ by Rietveld refinement and maximum entropy method analysis, *Solid State Commun.* 149 (2009) 41–44.
 - [37] P. Scherrer, Göttinger Nachrichten Gesell., 1918, vol. 2, Search PubMed, 98.
 - [38] N.D.S. Mohallem, G.L.T. Nascimento, J.B. Silva, V.L. Guimarães, Study of Multifunctional Nanocomposites Formed by Cobalt Ferrite Dispersed in a Silica Matrix Prepared by Sol-gel Process, INTECH Open Access Publisher, 2012.
 - [39] Z. Wang, R. Downs, V. Pischcheda, R. Shetty, S. Saxena, C. Zha, Y. Zhao, D. Schiferl, A. Waskowska, High-pressure x-ray diffraction and Raman spectroscopic studies of the tetragonal spinel CoFe_2O_4 , *Phys. Rev. B* 68 (2003) 094101.
 - [40] B. Raveau, M. Seikh, Cobalt Oxides: From Crystal Chemistry to Physics, John Wiley & Son, 2012.
 - [41] T.J. Inoue, *J. Electrochem. Soc. Jpn.* (1955) 24.
 - [42] C. Liu, A.J. Rondinone, Z.J. Zhang, Synthesis of magnetic spinel ferrite CoFe_2O_4 nanoparticles from ferric salt and characterization of the size-dependent superparamagnetic properties, *Pure Appl. Chem.* 72 (2000) 37–45.
 - [43] R.A. Patrick, G. Van Der Laan, C.M.B. Henderson, P. Kuiper, E. Dudzik, D.J. Vaughan, Cation site occupancy in spinel ferrites studied by X-ray magnetic circular dichroism developing a method for mineralogists, *Eur. J. Mineral.* 14 (2002) 1095–1102.
 - [44] Y. Qu, H. Yang, N. Yang, Y. Fan, H. Zhu, G. Zou, The effect of reaction temperature on the particle size, structure and magnetic properties of coprecipitated CoFe_2O_4 nanoparticles, *Mater. Lett.* 60 (2006) 3548–3552.
 - [45] Y. Zhang, Z. Yang, D. Yin, Y. Liu, C. Fei, R. Xiong, J. Shi, G. Yan, Composition and magnetic properties of cobalt ferrite nano-particles prepared by the co-precipitation method, *J. Magn. Magn. Mater.* 322 (2010) 3470–3475.
 - [46] H. Le Trong, T.M.A. Bui, L. Presmanes, A. Barnabé, I. Pasquet, C. Bonningue, P. Tailhades, Preparation of iron cobaltite thin films by RF magnetron sputtering, *Thin Solid Films* 589 (2015) 292–297.
 - [47] I.S. Molchan, G.E. Thompson, R. Lindsay, P. Skeldon, V. Likodimos, G.E. Romanos, P. Falaras, A. Adamova, B. Iliev, T.J. Schubert, Corrosion behaviour of mild steel in 1-alkyl-3-methylimidazolium tricyanomethanide ionic liquids for CO_2 capture applications, *RSC Adv.* 4 (2014) 5300–5311.
 - [48] C.-W. Tang, C.-B. Wang, S.-H. Chien, Characterization of cobalt oxides studied by FT-IR, Raman TPR and TG-MS, *Thermochim. Acta* 473 (2008) 68–73.
 - [49] G. Dascalu, D. Durneata, O.F. Caltun, Magnetic measurements of RE-doped cobalt ferrite thin films, *Magnet. IEEE Trans.* 49 (2013) 46–49.
 - [50] M. Descostes, F. Mercier, N. Thomat, C. Beaucaire, M. Gautier-Soyer, Use of XPS in the determination of chemical environment and oxidation state of iron and sulfur samples: constitution of a data basis in binding energies for Fe and S reference compounds and applications to the evidence of surface species of an oxidized pyrite in a carbonate medium, *Appl. Surf. Sci.* 165 (2000) 288–302.
 - [51] S. Diodati, S. Gross, Coprecipitated transition metal ferrites investigated by XPS, *Surf. Sci. Spectra* 20 (2013) 17–34.
 - [52] T. Yamashita, P. Hayes, Analysis of XPS spectra of Fe^{2+} and Fe^{3+} ions in oxide materials, *Appl. Surf. Sci.* 254 (2008) 2441–2449.
 - [53] M.I. Dar, S.A. Shivashankar, Single crystalline magnetite, maghemite, and hematite nanoparticles with rich coercivity, *RSC Adv.* 4 (2014) 4105–4113.
 - [54] A.N. Mansour, R.A. Brizzolara, Characterization of the surface of $\alpha\text{-FeOOH}$ powder by XPS, *Surf. Sci. Spectra* 4 (1996) 357–362.
 - [55] S. Ladas, L. Sygellou, S. Kennou, M. Wolf, G. Roeder, A. Nutsch, M. Rambach, W. Lerch, An X-ray photoelectron spectroscopy study of ultra-thin oxynitride films, *Thin Solid Films* 520 (2011) 871–875.
 - [56] S.-H. Do, J.-H. Jo, Y.-H. Jo, H.-K. Lee, S.-H. Kong, Application of a peroxy-monosulfate/cobalt (PMS/Co (II)) system to treat diesel-contaminated soil, *Chemosphere* 77 (2009) 1127–1131.
 - [57] G.P. Anipsitakis, Cobalt-mediated activation of peroxymonosulfate and sulfate radical attack on phenolic compounds. Implications of chloride ions, *Environ. Sci. Technol.* 40 (2006) 1000–1007.
 - [58] Y. Ren, L. Lin, J. Ma, J. Yang, J. Feng, Z. Fan, Sulfate radicals induced from peroxymonosulfate by magnetic ferrosin MFe_2O_4 ($\text{M} = \text{Co}, \text{Cu}, \text{Mn}$, and Zn) as heterogeneous catalysts in the water, *Appl. Catal. B: Environ.* 165 (2015) 572–578.
 - [59] J.A. Khan, X. He, H.M. Khan, N.S. Shah, D.D. Dionysiou, Oxidative degradation of atrazine in aqueous solution by UV/ H_2O_2 / Fe^{2+} , UV/ Fe^{2+} and UV/ Fe^{2+} processes: a comparative study, *Chem. Eng. J.* 218 (2013) 376–383.
 - [60] X. Pang, Y. Guo, Y. Zhang, B. Xu, F. Qi, LaCoO_3 perovskite oxide activation of peroxy-monosulfate for aqueous 2-phenyl-5-sulfobenzimidazole degradation: effect of synthetic method and the reaction mechanism, *Chem. Eng. J.* 304 (2016) 897–907.
 - [61] J. Mi, J. Ren, Y. Zhang, Preparation of modified semi-coke-supported ZnFe_2O_4 sorbent with the assistance of ultrasonic irradiation, *Environ. Eng. Sci.* 29 (2012) 1026–1031.
 - [62] J. Dona, C. Garriga, J. Arana, J. Pérez, G. Colón, M. Macías, J. Navio, The effect of dosage on the photocatalytic degradation of organic pollutants, *Res. Chem. Intermed.* 33 (2007) 351–358.
 - [63] G.P. Anipsitakis, D.D. Dionysiou, Degradation of organic contaminants in water with sulfate radicals generated by the conjunction of peroxymonosulfate with cobalt, *Environ. Sci. Technol.* 37 (2003) 4790–4797.
 - [64] A. Farhat, J. Keller, S. Tait, J. Radjenovic, Removal of persistent organic contaminants by electrochemically activated sulfate, *Environ. Sci. Technol.* 49 (2015) 14326–14333.
 - [65] C. Liang, H.-W. Su, Identification of sulfate and hydroxyl radicals in thermally activated persulfate, *Ind. Eng. Chem. Res.* 48 (2009) 5558–5562.
 - [66] B.-T. Zhang, Y. Zhang, Y. Teng, M. Fan, Sulfate radical and its application in decontamination technologies, *Crit. Rev. Environ. Sci. Technol.* 45 (2014) 1756–1800.
 - [67] K. Tennakone, S. Punchihewa, R. Tantrigoda, Photocatalytic oxidation of nitrite in water to nitrate, *Environ. Pollut.* 57 (1989) 299–305.
 - [68] G. Zhang, E.M. Wurtzler, X. He, M.N. Nadagouda, K. O'Shea, S.M. El-Sheikh, A.A. Ismail, D. Wendell, D.D. Dionysiou, Identification of TiO_2 photocatalytic destruction byproducts and reaction pathway of cylindrospermopsin, *Appl. Catal. B: Environ.* 163 (2015) 591–598.
 - [69] S. Khan, X. He, J.A. Khan, H.M. Khan, D.L. Boccelli, D.D. Dionysiou, Kinetics and mechanism of sulfate radical- and hydroxyl radical-induced degradation of highly chlorinated pesticide lindane in UV/peroxymonosulfate system, *Chem. Eng. J.* 318 (2007).
 - [70] S. Song, M. Xia, Z. He, H. Ying, B. Lü, J. Chen, Degradation of p-nitrotoluene in aqueous solution by ozonation combined with sonolysis, *J. Hazard. Mater.* 144 (2007) 532–537.